

Development of successive karstic systems within the Baix Penedès Fault zone (onshore of the Valencia Trough, NW Mediterranean)

V. BAQUÉS, A. TRAVÉ AND I. CANTARERO

Departament de Geoquímica, Petrologia i Prospecció Geològica, Facultat de Geologia, Universitat de Barcelona (UB), Barcelona, Spain

ABSTRACT

The Baix Penedès Fault zone records successive karstic systems. The outcrops studied correspond to different segments of the fault, which were temporarily connected and disconnected, allowing for different diagenetic processes to occur. The first karstic system affected the Mesozoic rocks due to subaerial exposure after Paleogene compression, an event characterized by widespread dissolution and the generation of vug and cavern porosity. The $\delta^{18}\text{O}$ values of the dolomitic sediment filling the initial vuggy porosity are similar to those of the host dolomite, indicating that the sediment comes from the erosion and reworking of the host rock. The second karstic system is related to the upward propagation of the Baix Penedès Fault. This deformation was characterized by random-fracture fabrics with dolomite cement and sediment. The stable isotopes values and Sr/Ca ratios of both the dolomite cement and sediments are similar to those of the host rock. In contrast, the more depleted $\delta^{13}\text{C}$ values indicate the influence of soil-derived CO_2 and the opening of the system to meteoric waters. During the third karstic event, the $\delta^{18}\text{O}$, $\delta^{13}\text{C}$, Sr/Ca ratios, and $^{87}\text{Sr}/^{86}\text{Sr}$ values of diagenetic cements suggest a marine signature, indicating that the karstic sediments were dolomitized under the influence of late Burdigalian-Langhian marine waters. These marine waters were probably expelled from poorly buried sediments and circulated through faults producing dolomitization of the karstic sediments. A final karst system developed during a period of uplift and subaerial exposure. The $\delta^{18}\text{O}$ values, the Mg/Ca and Sr/Ca ratios, and the high radiogenic values of the calcite cements formed during this period indicate precipitation from meteoric waters. The results of this study have implications for carbonate hydrocarbon reservoir analogs subject to karstic influence in the Valencia Trough and elsewhere.

Key words: karstification, meteoric fluids, Neogene, normal faults, Penedès basin

Received 31 July 2012; accepted 19 May 2013

Corresponding author: V. Baqués, Departament de Geoquímica, Petrologia i Prospecció Geològica. Facultat de Geologia. Universitat de Barcelona (UB). c/ Martí i Franquès s/n, 08028 Barcelona, Spain.

Email: vbaques@ub.edu. Tel: +34934031165. Fax: +34934021340.

Geofluids (2014) 14, 75–94

INTRODUCTION

Karstic speleothems have been frequently used for climatic studies (Gascoyne 1992; Fairchild *et al.* 2006) as their laminated growth structure allows for the analysis of geochemical variations through time. Similarly, the minerals precipitated on the fracture walls reflect different fluid flow events along fracture pathways. Petrographic and geochemical ($\delta^{18}\text{O}$, $\delta^{13}\text{C}$, $^{87}\text{Sr}/^{86}\text{Sr}$ and trace element analyses) studies of fracture calcite have also been used for solving the variation in depth of the fresh/saline water interface and hence the long-term palaeohydrological behavior of a specific site (Tullborg *et al.* 2008).

On the other hand, studies related to shallow-water carbonate deposits demonstrate that water-level and climatic fluctuations are major controls on both the rate and the style of early, near-surface carbonate diagenesis (Esteban & Klappa 1983), recognizing repeated changes from marine to fresh-water conditions and phreatic to vadose environments (Csoma *et al.* 2004). All these diagenetic cycles can be used to assess the porosity evolution of a specific site.

The recognition of paleokarst in ancient carbonate sequences (James & Choquette 1988; Mussman *et al.* 1988) is of major significance for hydrocarbon exploration because it enhances porosity (Esteban & Wilson 1993). Moreover, fractures served as pathways for fluids forming

hypogenic caves as well as for hydrocarbons and for fluids mineralizing caves and fractures (Poros *et al.* 2012).

The Valencia Trough is a NE–SW oriented basin located between the Iberian Peninsula and the Balearic Islands. It belongs to the complex system of Neogene basins initially created in the Mediterranean by the Paleogene compression (early Eocene to late Oligocene) and finally developed and settled in the Neogene (early Miocene). An extensive paleokarst system developed within the Mesozoic rocks that surround the Neogene basins (Cabrera 1981; Albaigés *et al.* 1985; Lomando *et al.* 1993; Playà *et al.* 2010; Rodríguez-Morillas *et al.* 2013). This paleokarst is related to the Mesozoic/Tertiary unconformity, which resulted from subaerial exposure of Mesozoic rocks during the Paleogene orogeny and is recognized throughout the entire Mediterranean domain (Esteban 1991). The major petroleum system of the Iberian Peninsula is located on the offshore Mediterranean and is still considered one of the most prospective areas (Vera *et al.* 1988; Clavell & Berastegui 1991; Klimowitz *et al.* 2005; Varela *et al.* 2005). Furthermore, during the Messinian (5.96–5.35 Ma), the Mediterranean Sea became isolated from the world's oceans as the result of a large drop in sea level and widespread deposition of evaporites (Krijgsman *et al.* 1999). This drastic drop in base level affected the local karst systems, creating new karst systems or the reworking of the previous one, such as Cretaceous bauxite-filled fissures and caves (Combes 1969; Audra *et al.* 2004). The influence of the Messinian event has been widely recognized in France (Julian & Nicod 1984; Clauzon *et al.* 1997) and Italy (Bini *et al.* 1978; Bini 1994). In fact, the major porosity-creating process in the offshore Amposta Marino oilfield has been specifically attributed to mixing zone corrosion in a coastal setting during the Miocene, which enhanced a previous meteoric karst system (Wigley *et al.* 1988). Presented here are the results of an outcrop-based study of the footwall zone of the Baix Penedès Fault, which is very well exposed in the Penedès half-graben. This basin can serve as an outcrop analog to the basins existing in the offshore Mediterranean where oil fields developed. The study examines the different karstic dissolution and infilling events associated with the different fracture systems that formed in the Penedès half-graben during its evolution.

The objective of this study is to characterize the karstic processes occurred during the development of shallow deformation of these structures. The results of this study have implications for carbonate hydrocarbon reservoir analogs subject to karstification in the Valencia Trough and elsewhere.

GEOLOGICAL SETTING

The Catalan Coastal Ranges (CCR) (Fig. 1A) resulted from the superposition of three main tectonic events. (i) A Mesozoic extensional phase which is divided into two rif-

ting episodes, the first, Late Permian to Triassic in age, is related to the opening of the Neotethys and the second, latest Oxfordian to Aptian in age, is related to the opening of the North Central Atlantic Ocean and the Bay of Biscay (Salas & Casas 1993; Salas *et al.* 2001). (ii) A Paleocene to middle Oligocene compressional phase that generated the Catalan Intraplate Belt (CIB) from the inversion of the Mesozoic rift basins. This phase includes the emplacement of ENE-WSW to-NE-SW trending thick-skinned thrust sheets bound by SE-dipping thrusts with a limited left-lateral strike-slip motion (Ashauer & Teichmüller 1935; Llopis-Lladó 1947; Anadón *et al.* 1985; Guimerà 2004). (iii) The third tectonic event was the late Oligocene?–Neogene extensional phase that generated the extensional reactivation of the main Paleogene reverse faults of the CCR (Fontboté 1954; Gaspar-Escribano *et al.* 2004). These faults split the CIB into a set of ENE-WSW blocks tilted toward the NW, constituting the actual horst-and-graben systems present at the northwestern Mediterranean (Bartrina *et al.* 1992; Roca & Guimerà 1992).

The Penedès half-graben is located at the central part of the CCR (Fig. 1B). Two major structural highs surround this graben: Gaià-Montmell High and Garraf Horst which in turn include minor fault-bound depressions (Vilanova and Baix Llobregat). The horsts are made up of Mesozoic carbonates and, locally, siliciclastic and evaporitic rocks overlaying the Variscan basement. The NW margin of the graben is bound by the Vallès-Penedès Fault, with a vertical slip from 2 to 4 km (Roca *et al.* 1999) (Fig. 1C). Minor faults, up to a few hundred meters of displacement, make up the present southern boundary, separating the depression from the Garraf Horst. A karstified prerift unconformity (late Oligocene–early Miocene), associated with different weathering products (scree deposits, paleosoils), underlies the lowermost Neogene basin infill (Agustí *et al.* 1985). Three depositional complexes are distinguished filling the basin (Cabrera *et al.* 1991; Cabrera & Calvet 1996): (i) a lower continental complex consisting of thick red bed sequences deposited in alluvial fan environment, Aquitanian to early Burdigalian in age; (ii) a marine to transitional complex, late Burdigalian to Serravallian in age, with sabhka facies, carbonate platform facies and siliciclastic and bay facies; and (iii) an upper continental complex, late Serravallian–Tortonian in age, consisting of thick red bed sequences deposited in alluvial fan environments. These sediments are covered either by alluvial-fluvial units (Gallart 1981) and/or marine units (Martinell 1988) of lower Pliocene age onlapping a deeply entrenched Messinian erosive surface, which affected both the basement rocks and the earlier Neogene sequences.

METHODS

The structure, sedimentary fills and macroscopic diagenetic fabrics related to the Baix Penedès Fault, and its related

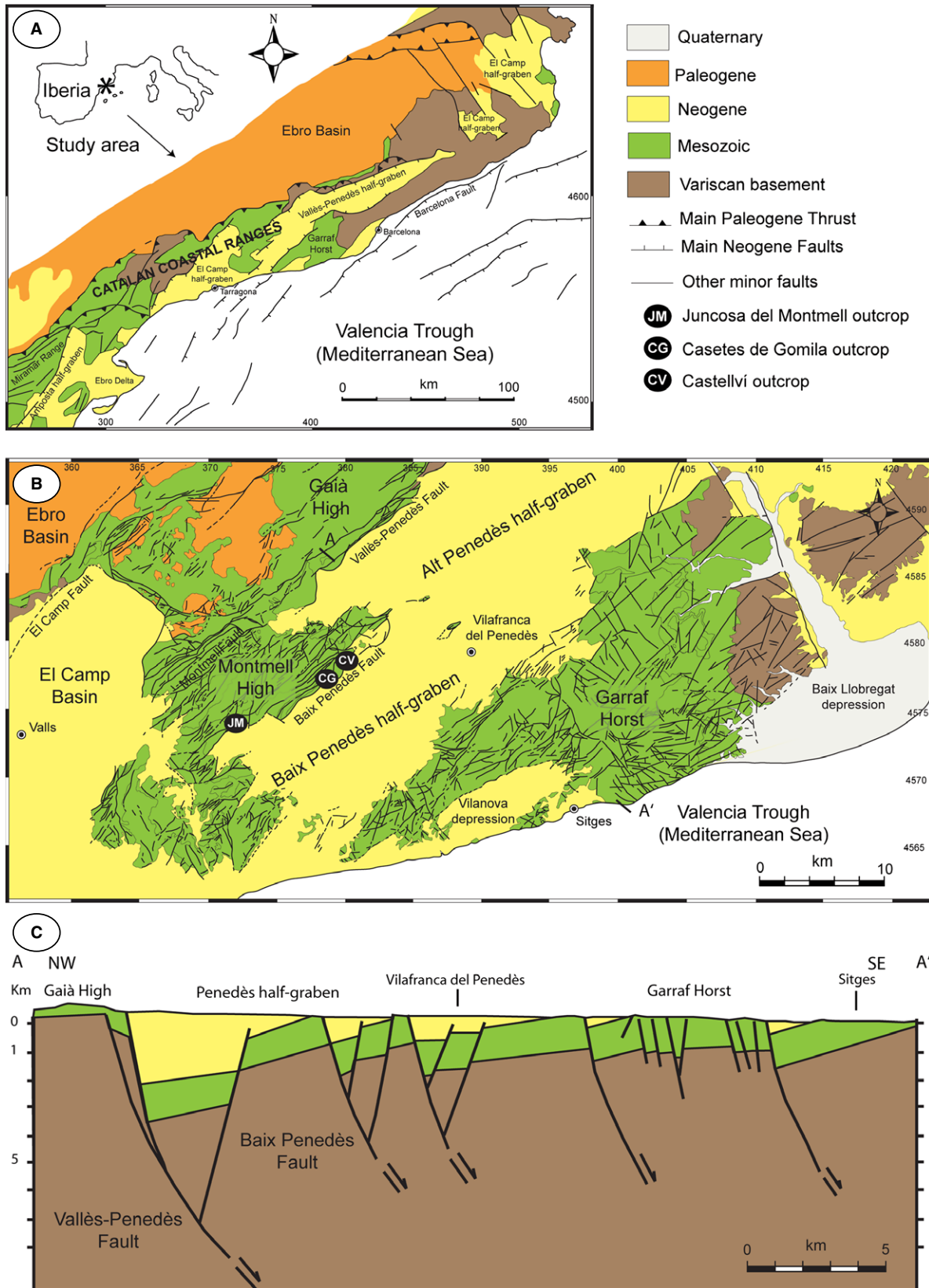


Fig. 1. (A) Regional geological map of the Catalan Coastal Ranges; (B) Geological map of the Penedès half-graben. The round points show the location of the studied outcrops; (C) Cross-section through the central part of the Penedès half-graben.

karstic features were measured and mapped. To characterize the evolution of the fluid flow, we combined a structural analysis with a petrological and mineralogical study of 33 standard and polished thin sections made from 27 hand samples collected both in the veins-filling fractures and in the host rocks. The thin sections were stained with Alizarine Red-S and potassium ferricyanide to distinguish calcite and dolomite from their ferroan equivalents (Dickson 1966). A Technosyn Cold Cathodoluminescence device (model 8200 MkII) operating at 15–18 Kv and 150–350 μ A current gun was used to distinguish the different cementations phases. The geochemical analysis of the calcite and dolomite cements and sediments (stable isotopes, elemental geochemistry, and $^{87}\text{Sr}/^{88}\text{Sr}$ ratios) allowed us to characterize the different fluids. The comparison of the cement geochemistry with the host rock carbonate geochemistry gave us clues regarding rock–fluid interaction. A fluid inclusion study was not carried out because of the virtual absence of fluid inclusions in the cements, probably due to the low temperature of precipitation. The host rock and veins-filling fractures were sampled for carbon- and oxygen-isotope analysis employing a 500- μ m-thick dental drill to extract 60 ± 10 μ g of powder from polished slabs. The calcite and dolomite powder was reacted with 103% phosphoric acid for 10 min at 90°C. The CO_2 was analyzed using an automated Kiel Carbonate Device attached to a Thermal Ionization Mass Spectrometer Thermo Electron (Finnigan) MAT-252. The results are precise to $\pm 0.02\%$ for $\delta^{13}\text{C}$ and $\pm 0.04\%$ for $\delta^{18}\text{O}$ and were corrected using the standard technique (Craig & Gordon 1965; Claypool *et al.* 1980), expressed in ‰ with respect to the VPDB (Vienna Pee Dee Belemnite) standard. The values for fluids are expressed relative to the VSMOW (Vienna Standard Mean Ocean Water) standard. The equation for conversion between the VPDB and VSMOW standards is $\delta^{18}\text{O}_{\text{VSMOW}} = 1.03091\delta^{18}\text{O}_{\text{VPDB}} + 30.91$ (Coplen *et al.* 1983).

Sr chromatography was performed using the method described by Pin & Bassin (1992) using Sr-resin commercially known as *Sr-Spec* and produced by Eichrom Laboratories. Sr isotope measurements were carried out in a Finnigan MAT-262 mass spectrometer. Samples were loaded onto a Ta filament (99.95%) previously degassed in two stages at 2 A and 4.5 A for 30 min. The measurement of isotopic ratios was carried out under the following conditions: ^{88}Sr beam intensity approximately 4V, achieving 20 blocks of 10 sweeps, and ^{85}Rb to monitor potential isobaric interferences. The analytical data were corrected by linear law mass fractionation using a constant ratio $^{86}\text{Sr}/^{88}\text{Sr} = 0.1194$ (Steiger & Jäger 1977). The analysis of strontium isotopes can be used to indirectly date carbonates or to give an indication of the importance of water/rock interactions in the system. Strontium isotopic ratios of seawater are very well constrained, and the varia-

tion though time of this ratio allowed us constrain a specific age for a given ratio (Burke *et al.* 1982; Howarth & McArthur 1997; Veizer *et al.* 1999; McArthur *et al.* 2001). Moreover, when diagenetic processes occur from nonmodified seawater, the $^{87}\text{Sr}/^{86}\text{Sr}$ ratio of the diagenetic products helps to constrain the age of the diagenetic processes.

Carbon-coated polished thin sections were used to analyze minor and trace element concentrations on a CAMECA SX-50 electron microprobe. The microprobe was operated using 20 Kv excitation potential, a current intensity of 15 nA and a beam diameter of 10 μ m. The detection limits were 99 ppm for Mn, 144 ppm for Fe, 103 ppm for Na, 386 ppm for Mg, 89 ppm for Sr ppm, and 497 ppm for Ca. Precision on major element analyses averaged 6.32% standard error at 3 sigma confidence levels.

FIELD OBSERVATIONS

The Baix Penedès Fault, well exposed at Castellví de la Marca (Baix Penedès), is a normal fault trending NE–SW and dipping toward the SE with a sub-vertical displacement of up to 1 km (Fig. 1C). This normal fault is related to the opening of the Valencia Trough during the Miocene (Roca *et al.* 1999; Marín *et al.* 2008) and put the Mesozoic dolomites of the footwall in contact with the upper continental complex of the middle Serravallian-Tortonian hanging wall. Within its footwall, the main fault is bound by a damage zone (Caine *et al.* 1996) several hundred meters wide, characterized by intense fracturation and brecciation (Baqués *et al.* 2010). In the fault core zone, the karst system is best developed. The architecture of the fractures and the diagenetic products that occur in the karst system and in the fault zone is described in the following sections.

Structure of the fault zone and fractures

We studied three outcrops across the Baix Penedès Fault, all situated within the footwall block. Throughout the fault, the footwall is comprised of the Garraf Upper Dolomites Formation of Thitonian-Berriasian age (Salas 1987). The Juncosa del Montmell outcrop is located near the southwest fault termination on a secondary road from La Bisbal del Penedès to La Juncosa del Montmell. The road cut exhibits a one hundred-meter-wide fresh section orthogonal to the fault plane between the undeformed dolomites of the footwall and the main fault plane. The Casetes de Gomila and Castellví outcrops are located along the central part of the fault, near Castellví de la Marca village. Both outcrops are relatively unweathered and are about five to ten meters-wide and orthogonal to the fault plane of the footwall block.

Along the Juncosa del Montmell outcrop, gray dolomites are found in 1.5-meter-thick beds trending N40 and dipping 10° northwest. The damage zone is several hundred meters wide and is characterized by random-fracture fabrics that generate a cemented crackle-to-mosaic packbreccia (field breccia classification by Morrow 1982) (Fig. 2). Various second-order faults are present within the damage zone involving up to fifty-centimeter-thick-cemented rubble packbreccia corresponding to the core zone. At the nearest part of the main fault, the core zone is about ten meters thick and is characterized by random fractures generating a cemented mosaic floatbreccia with dolomite sediments and calcite cements infilling the fractures. A final fracture system, trending NNW to SSE and dipping 70–80° northwest, cuts the Baix Penedès Fault zone. These fractures range in width from 2 to 40 cm with subangular walls. They are partially infilled by calcite sediments and cements. The sediments represent infiltration of carbonate mud. By contrast, the cements are new crystalline material precipitated within the sediment pores.

The Casetes de Gomila and Castellví outcrops are located in a relay zone of two different segments of the Baix Penedès Fault. The Casetes de Gomila outcrop exposes a five to ten meter-wide fault zone of Thitonian-Berriasian dolomites unconformably overlapped by the Miocene upper continental complexes (Fig. 3A). The dol-

omites are arranged in 0.2 to 1-meter-thick beds trending N70 and dipping 10° northwest at a distance from the main fault plane and 40° southeast close to the fault plane, forming an anticline forced by the normal motion of the Baix Penedès Fault. The undeformed footwall is not recognized in this outcrop. The damage zone, due to intense fracturation, exhibits a crackle-to-mosaic packbreccia recognizable up to fifty meters away from the main fault plane. Closer to the fault plane, the core zone is arranged into different lenses of cemented rubble floatbreccias with dolomitic sediments and cements.

The Castellví outcrop exposes up to thirty meters of the Baix Penedès Fault and a five to ten meter-wide fault zone orthogonal to the slip plane (Fig. 4). The fault plane is curved trending from N60 to N10 and ends toward another fault segment trending N60. This geometry corresponds to a classical connection between two segments of the normal fault generating a relay zone due to its propagation (Bellahsen & Daniel 2005). The dolomites are distributed in 0.3 to 1.5 meter-thick beds trending N40 and dipping 10° to the northwest. Nearer to the main fault plane, the bedding dips 10° southeastwards, forming a slight anticline forced by the normal motion of the Baix Penedès Fault as also occurred in the Casetes de Gomila outcrop. The damage zone consists of cemented crackle-to-mosaic packbreccia several meters along the footwall

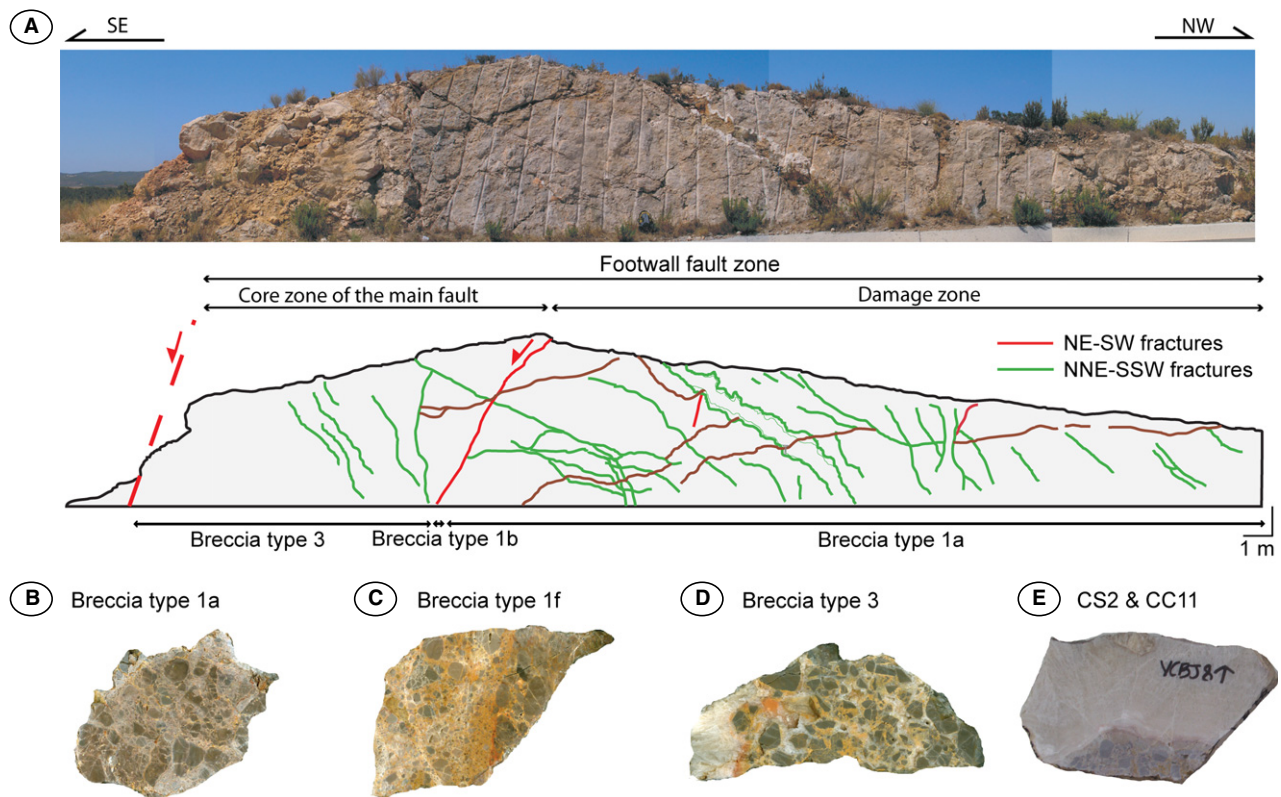


Fig. 2. Sketch of the Juncosa del Montmell outcrop showing the distribution of fractures, breccias and cements within the footwall of the Baix Penedès Fault.

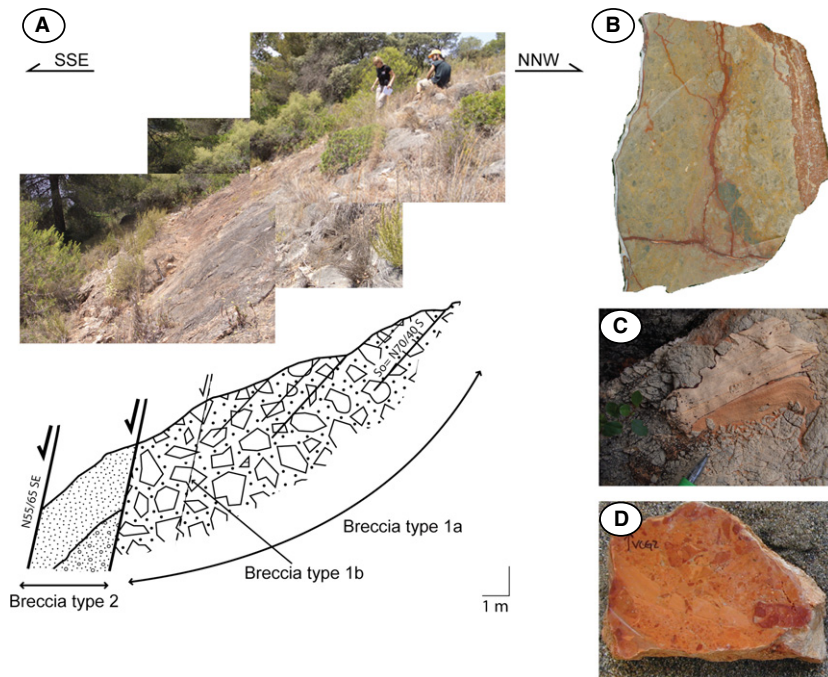


Fig. 3. Fault breccias and karstic laminated fillings within the footwall block of the Baix Penedès Fault cropping out at Casetes de Gomila location.

block and cemented rubble floatbreccia nearer the main fault. The core zone architecture is complex, characterized by random fractures partially filled by different types of dolomite sediments and by different layers of breccias parallel to the fault plane, which in turn is affected by the normal fault. A late fracture system, trending NNW to SSE and dipping 70–88° northwest, cuts the Baix Penedès Fault zone.

PETROLOGY AND GEOCHEMISTRY

The mesostructural description of the three outcrops allows us to recognize five different types of common deformation patterns: (i) three different systems of random fractures; (ii) NE–SW and (iii) NNW–SSE trending normal faults; (iv) related fault rocks (different types of breccias); and (v) karstic fillings (different types of sediments and cements). In this section, we will describe the petrologic and geochemical characteristics of these common deformation products and establish their relative chronology based on their crosscutting relationships. Figure 5 shows the paragenetic sequence from Mesozoic to present of the Baix Penedès Fault, indicating the different features observed in each outcrop. Below we will use the following nomenclature to describe the different diagenetic materials: RD, replacement dolomite; DS, dolomite sediment; CS, calcite sediment; DC, dolomite cement; CC, calcite cement. The different type of diagenetic materials are numbered according to their relative chronology.

Host rock (replacive dolomite RD1)

The dolomites consist of replacive dolomicrite to dolospa-rite with penetrative and destructive or nondestructive fabrics (RD1) (Fig. 6A). Ooids, ghosts of the original limestone, are locally recognized. The dolomite crystals are anhedral to subhedral, 10–150 μm in size and show dull purple luminescence (Fig. 6B). $\delta^{18}\text{O}$ varies from -2.1 to $+1.2$ ‰ VPDB and $\delta^{13}\text{C}$ from $+1$ to $+2.3$ ‰ VPDB (Fig. 7 & Table 1). The $^{87}\text{Sr}/^{86}\text{Sr}$ ratio is 0.707417 (Fig. 8 & Table 2), and the elemental composition is between 21.3 and 23.68% Ca, 12.03 and 13.57% Mg, and between 129 and 1148 ppm Sr, with Na, Mn, and Fe contents ranging from below detection limit to 921, 188, and 2306 ppm, respectively (Table 3).

Dolomitic sediment DS1

The first dissolution process was favored by the interstrata discontinuities, which generated vug porosity subparallel to bedding. This porosity was filled by dolomitic sediment DS1 consisting of dull orange luminescent anhedral dolomite crystals 25–150 μm in size (Fig. 6A–B). $\delta^{18}\text{O}$ varies from -1 to -0.6 ‰ VPDB, $\delta^{13}\text{C}$ from -3.2 to -2 ‰ VPDB (Fig. 7 & Table 1); Ca varies from 21.27 to 24.43%, Mg from 11.4 to 13.32%, and Sr from 364 to 1228 ppm. Na, Mn, and Fe contents range from below detection limit to 1316, 375, and 5906 ppm, respectively (Table 3).

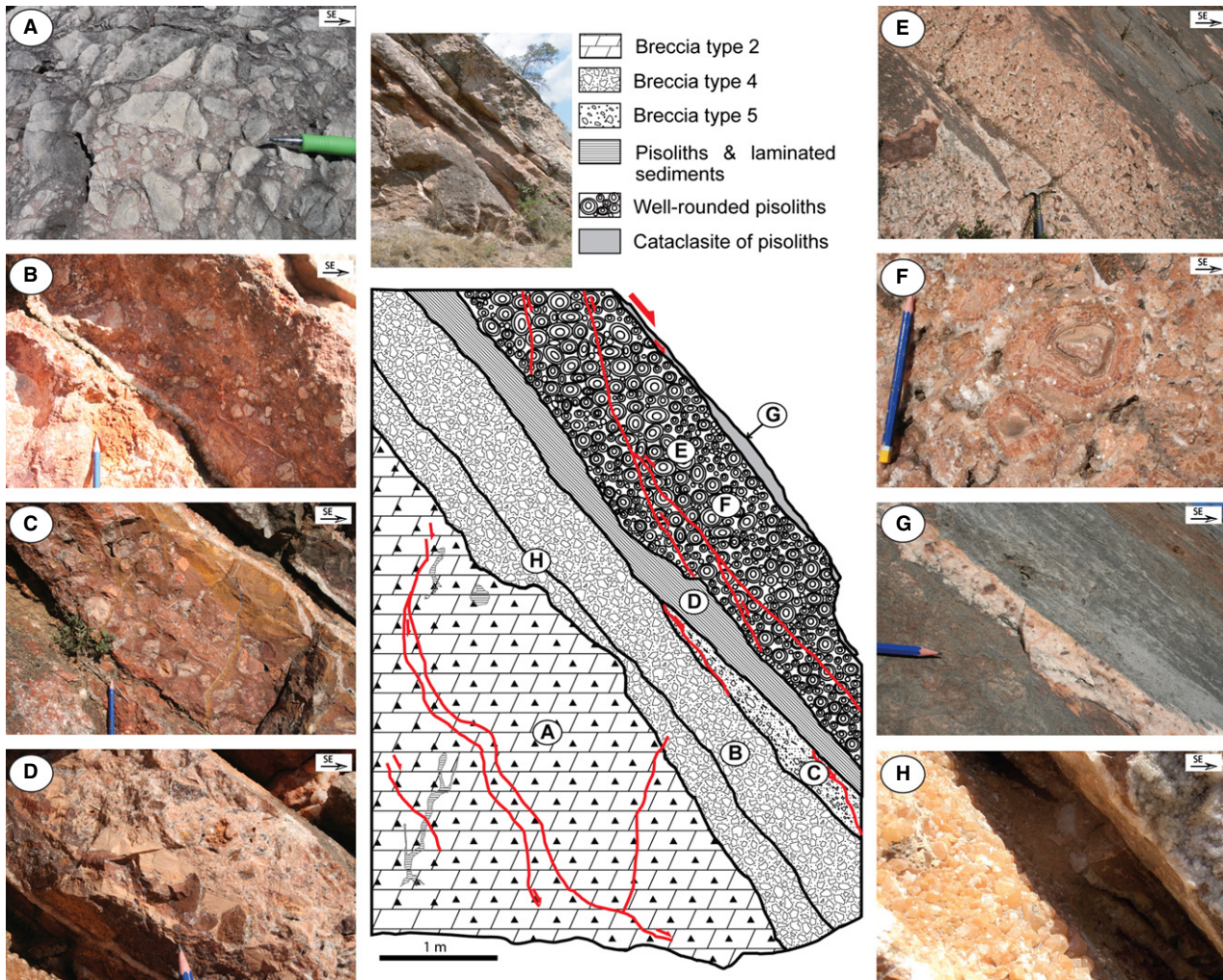


Fig. 4. Field photograph and scheme of the Castellví outcrop showing different karstic features: (A) Breccia type 2 and dolomitic sediment DS3; (B) Breccia type 4 and hematite cement H2; (C) Breccia type 5 and calcite cements CC3 to CC7; (D) Spelean pisoids, calcite cement CC8 and laminated sediment CS1; (E) Well-rounded spelean pisoids and calcite cements CC9 and CC10; (F) Detailed view of well-rounded spelean pisoids; (G) Cataclasite of spelean pisoids; (H) Calcite cement CC11.

Breccia type 1, dolomite cement DC1, and replacive dolomite RD2

As mentioned above, along the damage zone, the host rock is highly fractured. The fractures are mode I (opening) with no preferred orientation, 10–75 μm thick, and with subangular walls. Due to the intensity of fracturing, the damage zone consist of a cemented crackle-to-mosaic packbreccia (breccia type 1a) formed by angular fragments of dolomitic rocks, 0.5–4 cm in size (Fig. 2 & 3B). Both the fractures and the breccia are cemented by dolomitic cement DC1 made up of anhedral dull red luminescent crystals, 5–40 μm in size, growing in optical continuity with the host rock crystals (Fig. 6C–D). $\delta^{18}\text{O}$ varies from -2.3 to -0.4 ‰ VPDB and $\delta^{13}\text{C}$ from -0.8 to $+0.3$ ‰

VPDB (Fig. 7 & Table 1). Ca varies from 21.27 to 23.89%, Mg from 11.4 to 13.32%, and Sr from 314 to 952 ppm. Na, Mn, and Fe contents range from below the detection limit to 1316, 375, and 5908 ppm, respectively (Table 3). The core zone of secondary faults (up to 3–10 cm thick) consists of cemented rubble packbreccia (breccia type 1b) resulting from comminution of host dolomite, breccia type 1a, and DS1. Near the main fault plane, mainly in the core zone, DC1 is more abundant, and host dolomites are partially replaced by a dolosparite with penetrative and destructive fabric (RD2). The dolomite crystals are of subhedral habit and show dull to bright red luminescence. They are 50–300 μm in size (Fig. 6E–F), and their $\delta^{18}\text{O}$ varies from -4.6 to -0.7 ‰ VPDB and their $\delta^{13}\text{C}$ from -1 to $+1$ ‰ VPDB (Fig. 7 & Table 1).

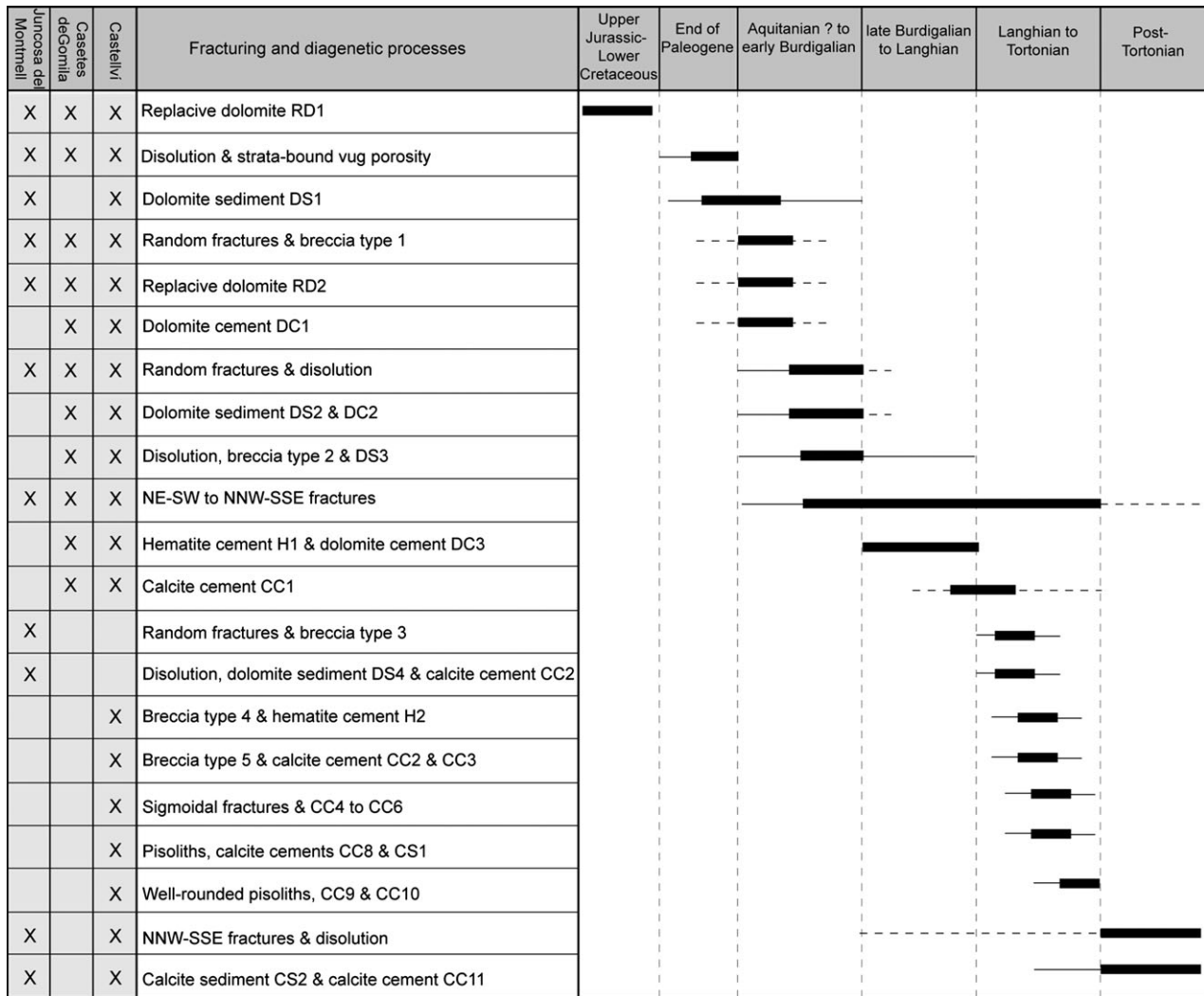


Fig. 5. Diagenetic sequence from Mesozoic to post-Tortonian times of the Baix Penedès Fault.

Dolomitic sediment DS2 and dolomitic cement DC2

Random fractures affect the brecciated footwall and the dolomitic sediment DS1. They are 75–400 μm thick with subangular walls and were apparently affected by intense dissolution, which generated channel and vug porosity (Fig. 3C). This porosity is filled by the orange dolomite sediment DS2, consisting of fragments of the host dolomite, 4–100 μm in size (Fig. 6). $\delta^{18}\text{O}$ varies from -1.8 to $+0.1$ ‰ VPDB, $\delta^{13}\text{C}$ from -4.2 to -2.9 ‰ VPDB (Fig. 7 & Table 1), and the $^{87}\text{Sr}/^{86}\text{Sr}$ ratio is 0.708761 (Fig. 8 & Table 2). The elemental composition is between 21.78 and 24.9% Ca, 10.6 and 13.12% Mg, and between 177 and 1250 ppm Sr, with Na, Mn, and Fe contents ranging from below the detection limit to 1130, 364 and 6927 ppm, respectively (Table 3). DS2 is cemented by DC2 arranged in rim position at the fracture walls or surrounding the host rock fragments (Fig. 6). The cement

has nonluminescent to orange luminescent zonation; its elemental composition is between 23.68 and 24.71% Ca, 10.61 and 12% Mg, between 258 and 476 ppm Na, between 218 and 2025 ppm Fe, and between 453 and 726 ppm Sr. Its Mn content ranges from below the detection limit to 211 ppm (Table 3).

Breccia type 2 and dolomitic sediment DS3

The continued dissolution processes, favored by the randomly oriented fractures, locally led to the collapse of fractures walls, originating the cemented rubble floatbreccia (breccia type 2) (Fig. 3D & 4A). This breccia consists of angular centimetric reworked fragments of host rock, dolomitic cements and sediments and is cemented by a pink to red dolomitic sediment (DS3). It is rich in iron oxides and is locally laminated (Fig. 3C). The sediment is made up of bright orange luminescent euhedral crystals,

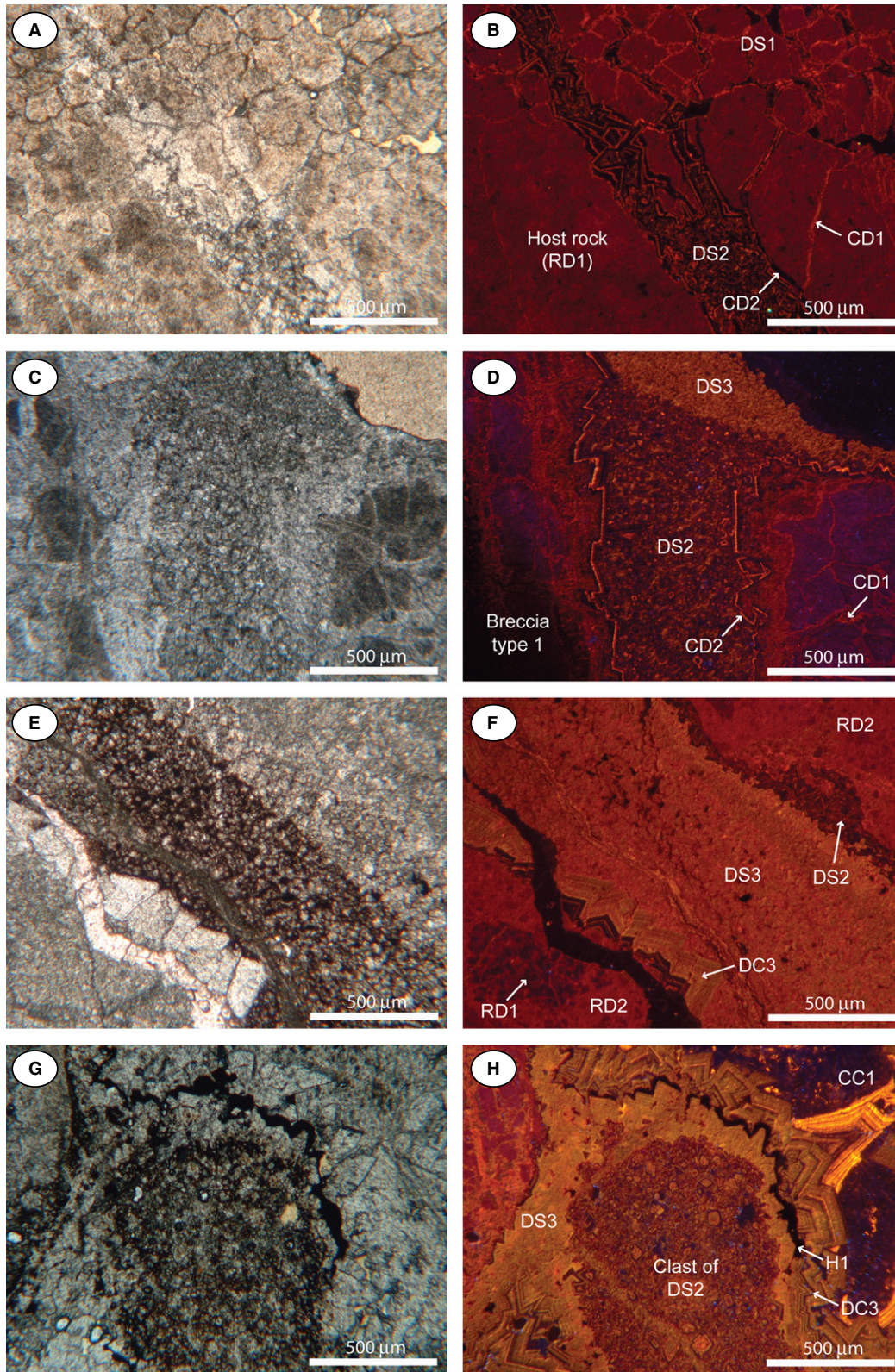


Fig. 6. (A & B) Host rock and dolomite sediment DS1 affected by irregular fractures and different fillings; (C & D) Crackle to mosaic packbreccia with dolomite cement DC1. Irregular fractures with dolomite sediments DS2, DS3 and dolomite cement DC3; (E & F) Replacive dolomite RD2 and fracture filled by dolomite sediments DS2, DS3 and dolomite cement DC3; (G & H) Breccia type 2 with reworked fragments of dolomitic sediments DS2 and DS3. Remaining vug porosity filled by hematite cement H1, dolomite cement DC3 and calcite cement CC1.

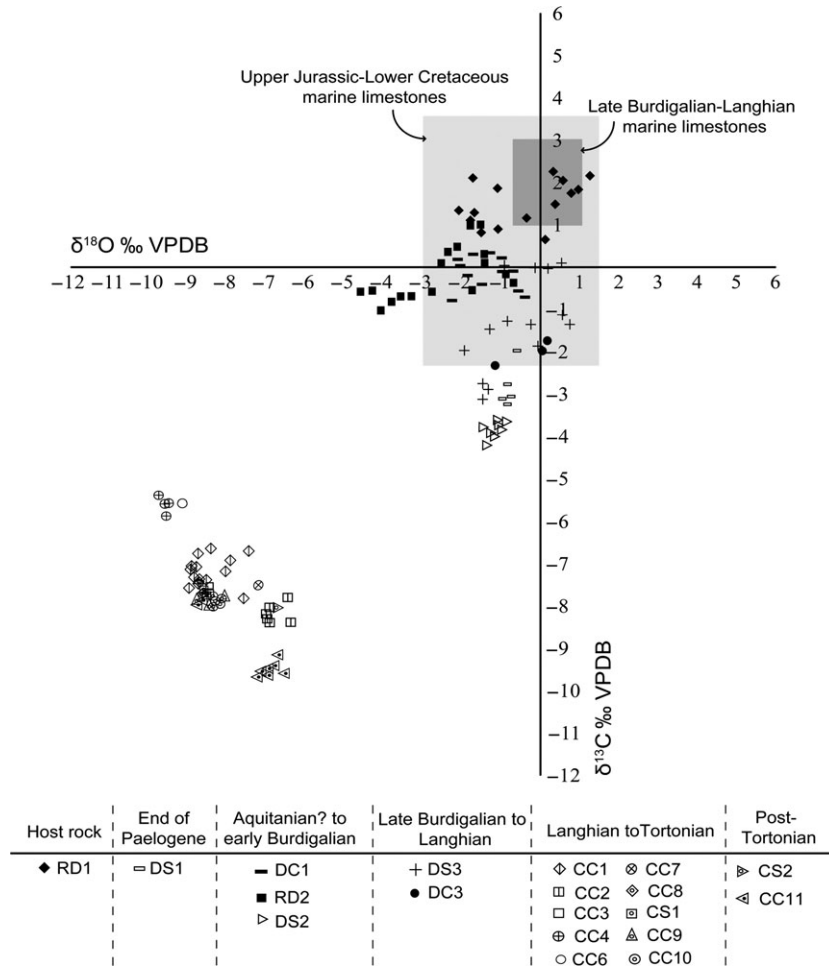


Fig. 7. $\delta^{18}\text{O}$ - $\delta^{13}\text{C}$ plot of host rocks and cements of the Baix Penedès Fault.

50–100 μm in size (Fig. 6E–F). $\delta^{18}\text{O}$ varies from -2 to $+0.7$ ‰ VPDB, $\delta^{13}\text{C}$ from -3.1 to $+0.1$ ‰ VPDB, and the $^{87}\text{Sr}/^{86}\text{Sr}$ ratio is 0.708855 (Figs. 7–8 & Tables 1–2). The elemental composition is between 22.35 and 24.43% Ca, 10.73 and 12.35% Mg, and between 237 and 1228 ppm Sr, with Na, Mn, and Fe contents ranging from below the detection limit to 484, 346, and 2866 ppm, respectively (Table 3).

Hematite cement H1 and dolomite cement DC3

The hematite and dolomite cements H1 and DC3, respectively, fill the NNW-SSE and NE-SW fractures (Fig. 3B). Hematite cement H1 is precipitated at one of the fracture walls and in the porosity remaining between dolomite sediment DS3 (Fig. 9A–B). DC3 is made up of zonally luminescent brown-orange euhedral crystals, 100–500 μm in size, growing along the c-axis, perpendicular to the fracture wall (Figs. 6A–F & 9A–B). The stable isotopes are -1.2 to $+0.1$ ‰ for $\delta^{18}\text{O}$ VPDB and -2.3 to -1.7 ‰

VPDB for $\delta^{13}\text{C}$ (Fig. 7 & Table 1). The elemental composition is between 22.52 and 24.49% Ca, 10.95 and 12.19% Mg, and between 115 and 1071 ppm Sr, with Na, Mn, and Fe contents ranging from below the detection limit to 611, 406, and 3197 ppm, respectively (Table 3).

Calcite cement CC1

In the Castellví outcrop, the remaining porosity, after the dolomite cement DC3 precipitation, was partially infilled by calcite cement CC1. This cement consists of subhedral crystals, 100–750 μm in size, showing bright-black orange-black luminescence zonation and featuring a blocky texture (Fig. 9a and 9b). $\delta^{18}\text{O}$ varies from -9 to -7.5 ‰ VPDB, $\delta^{13}\text{C}$ from -7.5 to -6.7 ‰ VPDB, and the $^{87}\text{Sr}/^{86}\text{Sr}$ ratio is 0.708293 (Figs. 7–8 & Tables 1–2). The elemental composition is between 39.02 and 40.27% Ca, 0.07 and 0.45% Mg; Na, Mn, Fe, and Sr contents range from below the detection limit to 330, 210, 273, and 491 ppm, respectively (Table 3).

Table 1 $\delta^{18}\text{O}$ and $\delta^{13}\text{C}$ values of the host-dolomite and the diagenetic products.

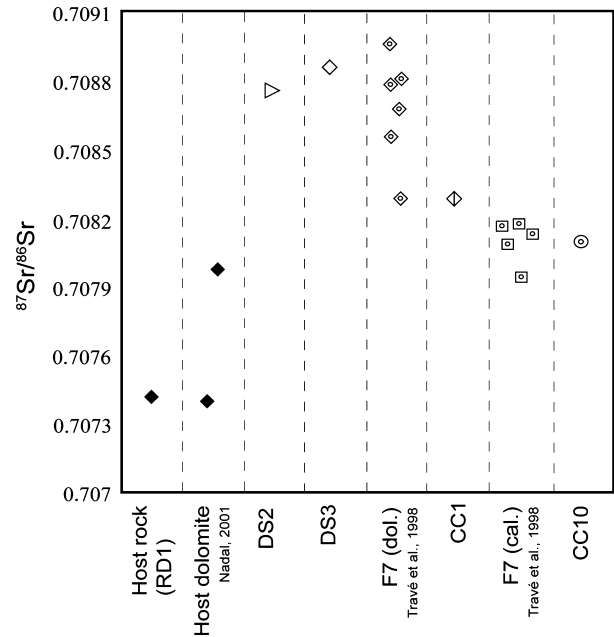
Filling stage		$\delta^{13}\text{C}$ ‰ VPDB	$\delta^{18}\text{O}$ ‰ VPDB
Host-dolomite RD1 <i>n</i> = 15	Min.	1	-2,1
	Max.	2,3	1,2
	Average	1,5	-0,5
Dolomite sediment DS1 <i>n</i> = 5	Min.	-3,2	-1,0
	Max.	-2,0	-0,6
	Average	-2,8	-0,8
Dolomite cement DC1 <i>n</i> = 12	Min.	-0,8	-2,3
	Max.	0,3	-0,4
	Average	-0,2	-1,4
Replacive dolomite RD2 <i>n</i> = 18	Min.	-1,0	-4,6
	Max.	1,0	-0,7
	Average	-0,1	-2,5
Dolomite sediment DS2 <i>n</i> = 11	Min.	-4,2	-1,8
	Max.	-2,9	0,1
	Average	-3,6	-1,1
Dolomite sediment DS3 <i>n</i> = 14	Min.	-3,1	-2,0
	Max.	0,1	0,7
	Average	-1,4	-0,6
Dolomite cement DC3 <i>n</i> = 3	Min.	-2,3	-1,2
	Max.	-1,7	0,1
	Average	-2,0	-0,4
Calcite cement CC1 <i>n</i> = 10	Min.	-7,5	-9,0
	Max.	-6,7	-7,5
	Average	-7,1	-8,5
Calcite cement CC2 <i>n</i> = 8	Min.	-8,3	-8,5
	Max.	-6,6	-6,4
	Average	-7,8	-7,2
Calcite cement CC3 <i>n</i> = 2	Min.	-7,5	-8,8
	Max.	-7,4	-8,6
	Average	-7,5	-8,7
Calcite cement CC4 <i>n</i> = 4	Min.	-5,9	-9,8
	Max.	-5,4	-9,5
	Average	-5,6	-9,2
Calcite cement CC6 <i>n</i> = 1	Min.		
	Max.		
	Average	-5,6	-9,2
Calcite cement CC7 <i>n</i> = 1	Min.		
	Max.		
	Average	-7,5	-7,2
Calcite cement CC8 <i>n</i> = 2	Min.	-7,7	-8,7
	Max.	-7,4	-8,6
	Average	-7,5	-8,7
Calcite cement CS1 <i>n</i> = 3	Min.	-7,8	-8,6
	Max.	-7,6	-8,5
	Average	-7,7	-8,6
Calcite cement CC9 <i>n</i> = 3	Min.	-7,9	-8,8
	Max.	-7,8	-8,1
	Average	-7,8	-8,4
Calcite cement CC10 <i>n</i> = 6	Min.	-7,9	-8,4
	Max.	-7,7	-8,1
	Average	-7,8	-8,3
Calcite cement CS2 <i>n</i> = 1	Min.		
	Max.		
	Average	-8,0	-6,9
Calcite cement CC11 <i>n</i> = 11	Min.	-9,6	-8,8
	Max.	-7,8	-6,5
	Average	-8,9	-7,4

Breccia type 3 and calcite cement CC2

In Juncosa del Montmell outcrop, the core zone of the main fault plane consists of 10-meter-thick-cemented mosaic-to-rubble packbreccia (Morrow 1982) (Fig. 2). This breccia (breccia type 3) is made up of subangular fragments

Table 2 $^{87}\text{Sr}/^{86}\text{Sr}$ ratios of the host-dolomite and the diagenetic products.

Filling stage	$^{87}\text{Sr}/^{86}\text{Sr}$
Host-dolomite RD1	0,707417
Dolomite sediment DS2	0,708761
Dolomite sediment DS3	0,708855
Calcite cement CC1	0,708293
Calcite cement CC10	0,708253


Fig. 8. $^{87}\text{Sr}/^{86}\text{Sr}$ of host rocks, cements and sediments present throughout the Baix Penedès fault zone. Data from Nadal (2001) and Travé *et al.* (1998) previous studies are included.

0.5–4 cm in size of reworked host dolomite and breccia type 1, and is cemented by two generations of fillings: internal dolomitic sediment (DS4), made up of subhedral to euhedral bright orange to bright yellow luminescent dolomitic crystals reworked from previous dolomitic sediments DS3 (Fig. 9 C–D). This sediment usually shows a thin depositional lamination and fills the lower part of the cavities. The second filling corresponds to calcite cement CC2, made up of subhedral crystals, 250 μm to 2 mm in size, and featuring a blocky texture (Fig. 9C–D). $\delta^{18}\text{O}$ varies from -8.5 to -6.4 ‰ VPDB, $\delta^{13}\text{C}$ from -8.3 to -6.6 ‰ VPDB (Fig. 7 & Table 1). The elemental composition is between 39.39 and 40.21% of Ca, between 0.12 and 0.27% of Mg, Na, Fe, and Sr contents ranges from below the detection limit to 312, 255, 273, and 482 ppm, respectively. The Mn content is always below to the detection limit (Table 3).

Breccia type 4 and hematite cement H2

Within the Castellví outcrop, overlying the karstified footwall zone is the breccia type 4, classified as particulate rubble floatbreccia (Morrow 1982) (Fig. 4B). This breccia is formed by angular mm to cm reworked fragments of host

Table 3 Minimum, maximum and average values of the elemental composition of the host-dolomite and diagenetic products and calculated Mg/Ca and Sr/Ca molar ratios of the parent fluid applying the distribution coefficient equation.

Filling stage	Mg (ppm)	Ca (ppm)	Na (ppm)	Mn (ppm)	Fe (ppm)	Sr (ppm)	Molar ratio Sr/Ca fluid (a)	Molar ratio Mg/Ca fluid (b)	Molar ratio Mg/Ca fluid (c)	Molar ratio Mg/Ca fluid (d)	Molar ratio Sr/Ca fluid (e)	Molar ratio Sr/Ca fluid (f)	Molar ratio Ca/Fe fluid (g)	Molar ratio Mn/Ca fluid (h)
Host-dolomite RD1 n = 88	Min.	12.03	21.30	0	0	129	0.00763							
	Max.	13.57	23.68	921	188	2306	0.07425							
	Average	12.80	22.06	243	36	359	0.04639							
Dolomite sediment DS1 n = 77	Min.	11.40	21.27	0	0	364	0.02684							
	Max.	13.32	24.43	1316	375	5908	0.06466							
	Average	12.66	22.12	174	73	1061	0.04546							
Dolomite cement DC1 n = 49	Min.	11.40	21.27	0	0	364	0.00573							
	Max.	13.32	23.89	1316	375	5908	0.06836							
	Average	12.68	22.06	169	70	1040	0.04264							
Dolomite sediment DS2 n = 74	Min.	10.60	21.78	0	0	52	0.00584							
	Max.	13.12	24.90	1130	364	6927	0.05316							
	Average	11.71	23.37	297	72	1399	0.03166							
Dolomite cement DC2 n = 6	Min.	10.62	23.68	258	75	218	0.01604							
	Max.	12.00	24.72	476	211	2025	0.02595							
	Average	11.36	24.28	396	146	911	0.02052							
Dolomite sediment DS3 n = 31	Min.	10.73	22.35	0	0	76	0.00792							
	Max.	12.35	24.43	484	346	2866	0.06390							
	Average	11.50	23.64	252	73	950	0.03016							
Dolomite cement DC3 n = 35	Min.	10.95	22.52	0	0	16	0.004768							
	Max.	12.19	24.49	611	406	3197	0.039275							
	Average	11.50	23.75	282	112	484	0.025944							
Calcite cement CC1 n = 8	Min.	0.07	39.02	0	0	0	0.22712	0.09734	0.02343	0.02083	0.00703	0	0	0
	Max.	0.45	40.27	330	210	273	1.60043	0.68590	0.16513	0.02083	0.00703	0	0	0
	Average	0.28	39.64	142	65	100	0.98623	0.42267	0.10176	0.00945	0.00319	0	0	0
Calcite cement CC2 n = 10	Min.	0.12	39.39	0	0	0	0.39780	0.17048	0.04105	0	0	0	0	0
	Max.	0.27	40.21	312	35	255	0.93569	0.40101	0.09655	0.02074	0.00700	0	0	0
	Average	0.18	39.74	100	10	86	0.62892	0.26954	0.06489	0.00867	0.00293	0	0	0
Calcite cement CC3 n = 13	Min.	0.13	39.41	0	0	0	0.46717	0.20021	0.04820	0	0	0	0	0
	Max.	0.56	40.28	262	253	655	1.92078	0.82319	0.19819	0.02184	0.00737	0	0	0
	Average	0.35	39.73	89	46	153	1.21922	0.52252	0.12580	0.01348	0.00455	0	0	0
Calcite cement CC4 n = 10	Min.	0.14	39.27	0	0	45	0.50026	0.21440	0.05162	0.00173	0.00058	0	0	0
	Max.	0.45	40.23	272	180	643	1.53351	0.65722	0.15823	0.02814	0.00950	0	0	0
	Average	0.28	39.78	91	61	289	0.96284	0.41265	0.09935	0.01332	0.00449	0	0	0
Calcite cement CC5 n = 9	Min.	0.07	39.05	13	0	84	0.23433	0.10043	0.02418	0.00213	0.00072	0	0	0
	Max.	0.42	40.13	185	164	478	1.45286	0.62266	0.14991	0.01921	0.00648	0	0	0
	Average	0.23	39.64	121	60	238	0.81379	0.34877	0.08397	0.00990	0.00334	0	0	0
Calcite cement CC6 n = 8	Min.	0.13	38.31	0	0	801	0.46618	0.19979	0.04810	0.00761	0.00257	0	0	0
	Max.	0.46	40.38	193	214	6564	1.57853	0.67651	0.16287	0.01888	0.00637	0	0	0
	Average	0.29	39.18	100	62	3076	1.00618	0.43122	0.10382	0.01328	0.00448	0	0	0
Calcite cement CC7 n = 6	Min.	0.04	39.17	0	0	57	0.15749	0.06750	0.01625	0.00255	0.00086	0	0	0
	Max.	0.15	40.32	327	160	541	0.50700	0.21729	0.05231	0.02602	0.00878	0	0	0
	Average	0.09	39.90	132	81	223	0.30793	0.13197	0.03177	0.01357	0.00458	0	0	0
Calcite cement CC8 n = 9	Min.	0.17	39.72	0	0	72	0.59045	0.25305	0.06092	0.00307	0.00104	0	0	0
	Max.	0.39	40.47	253	139	216	1.31784	0.56479	0.13598	0.02098	0.00708	0	0	0
	Average	0.26	40.00	78	46	83	0.89627	0.38411	0.09248	0.01356	0.00458	0	0	0

Table 3. (Continued)

Filling stage	Mg (ppm)	Ca (ppm)	Na (ppm)	Mn (ppm)	Fe (ppm)	Sr (ppm)	Molar ratio Sr/Ca fluid (a)	Molar ratio Mg/Ca fluid (b)	Molar ratio Mg/Ca fluid (c)	Molar ratio Mg/Ca fluid (d)	Molar ratio Sr/Ca fluid (e)	Molar ratio Sr/Ca fluid (f)	Molar ratio Ca/Fe fluid (g)	Molar ratio Mn/Ca fluid (h)
Calcite sediment CS1 n = 8	0.19	39.10	93	0	212	108		0.67280	0.28834	0.06942	0.00468	0.00158	515	0
	0.36	40.01	310	128	2885	686		1.24313	0.53277	0.12827	0.02906	0.00981	39	0.00001
	Average	0.28	39.54	174	41	1087	398		0.41979	0.10107	0.01707	0.00576	102	0.00001
Calcite cement CC9 n = 47	0.11	38.15	0	0	0	109		0.38671	0.16573	0.03990	0.00484	0.00163	0	0
	1.13	40.29	452	297	842	2146		3.84251	1.64679	0.39648	0.09026	0.03046	7900	0.00007
	Average	0.46	39.32	161	69	153	1068		1.59679	0.68434	0.16476	0.04602	0.01553	3950
Calcite sediment CS2 n = 5	0.31	38.83	0	0	46	1082		1.08379	0.46448	0.11183	0.04690	0.01583	193	0
	0.49	39.43	163	0	561	1207		1.72794	0.74054	0.17829	0.05229	0.01765	2374	0
	Average	0.40	39.15	61	0	306	1134		1.40946	0.60406	0.14543	0.04908	916	0
Calcite cement CC11 n = 19	0.11	38.59	0	0	0	1126		0.38066	0.16314	0.03928	0.04815	0.01625	0	0
	0.82	40.23	211	68	1103	1510		2.90118	1.24336	0.29935	0.06631	0.02238	1904	1.5839E-05
	Average	0.39	39.45	83	19	182	1304		1.35186	0.57937	0.13949	0.05606	952	4.31801E-06

n, number of analyzed spots in the same sample. a: KMg = 0.012 at 25°C (Mucci, 1987). b: KMg = 0.1163 at 90°C (Katz, 1973). c: KSr = 0.027 at 25°C (Lorens, 1981). d: KSr = 0.08 at 100–150°C (Kinsman, 1969). e: KFe = 5 at 25°C (Tucker and Wright, 1990).

rock and previous karstic fillings. The matrix contains reworked fragments of the dolomite sediments DS2 and DS3. Surrounding the reworked dolomite crystals is hematite cement H2 (Fig. 9E). This breccia is cemented by the calcite with the same petrography features and geochemistry signature as the cement CC2.

Breccia type 5 and calcite cements CC3, CC4, CC5, CC6 and CC7

Type 5 breccia corresponds to a cemented rubble floatbreccia (Morrow 1982) and is arranged parallel to the main fault plane cropping out at Castellví (Fig. 4C). This breccia is formed by subangular to subrounded fragments of the host rock, 1–3 cm in size. The breccia is composed of dolomitic sediments, and breccias of the previous stages. Some of these fragments are surrounded by a rim of bladed calcite cement CC3 (Fig. 9F). The cement $\delta^{18}\text{O}$ varies from -8.8 to -8.6 ‰ VPDB and $\delta^{13}\text{C}$ from -7.5 to -7.4 ‰ VPDB (Fig. 7 & Table 1). Elemental composition varies from 39.41 to 40.28% for Ca and 0.13 to 0.56% for Mg. Na, Mn, Fe, and Sr contents range from below the detection limit to 262, 253, 655 and 519 ppm respectively (Table 3). The breccia clasts are cemented by calcite cement CC4. This cement consists of nonluminescent subhedral crystals with goethite inclusions, 20–100 μm in size, featuring a blocky texture (Fig. 9F). The isotopic signal of CC4 cement varies from -9.8 to -9.5 for $\delta^{18}\text{O}$ and -5.9 to -5.4 for $\delta^{13}\text{C}$. (Fig. 7 & Table 1). Elemental composition varies from Mg 39.27 to 40.23 for Ca, 0.14 to 0.45% for Mg. The Na, Mn, Fe, and Sr contents range from below the detection limit to 272, 180, 643 and 668 ppm respectively (Table 3). Sigmoidal extensional fractures affect this breccia (Fig. 4C). The fractures are filled by three generations of cements (CC5, CC6, and CC7). The calcite cement CC5 is made up of non-luminescent anhedral calcite crystals, 25–50 μm in size, with a rim disposition (Ginsburg 1957) (Fig. 9F). Elemental composition of CC5 is between 39.05 and 40.13% for Ca and 0.07 and 0.42% for Mg. The Na, Mn, Fe and Sr contents range from below the detection limit to 185, 164, 478 and 455 ppm respectively (Table 3). The second calcite cement generation (CC6) corresponds to a yellow cement with a high amount of goethite inclusions. This cement consists of nonluminescent blocky subhedral calcite crystals, 50–150 μm in size (Fig. 9F). Its $\delta^{18}\text{O}$ is -9.2 ‰ VPDB and $\delta^{13}\text{C}$ is -5.6 ‰ VPDB (Fig. 7 & Table 1). Elemental composition range from 38.31 to 40.38% for Ca, 0.13 to 0.46% for Mg, 801 to 6564 ppm for Fe and between 172 to 450 ppm for Sr. The Na and Mn contents range from below the detection limit to 193 and 214 ppm respectively (Table 3). The third calcite cement (CC7) is made up of nonluminescent blocky euhedral crystals, 100–150 μm in size (Fig. 9F). The $\delta^{18}\text{O}$ value of CC7 is -7.2 ‰ VPDB and $\delta^{13}\text{C}$ is -7.5 ‰ VPDB (Fig. 7 & Table 1). Elemental com-

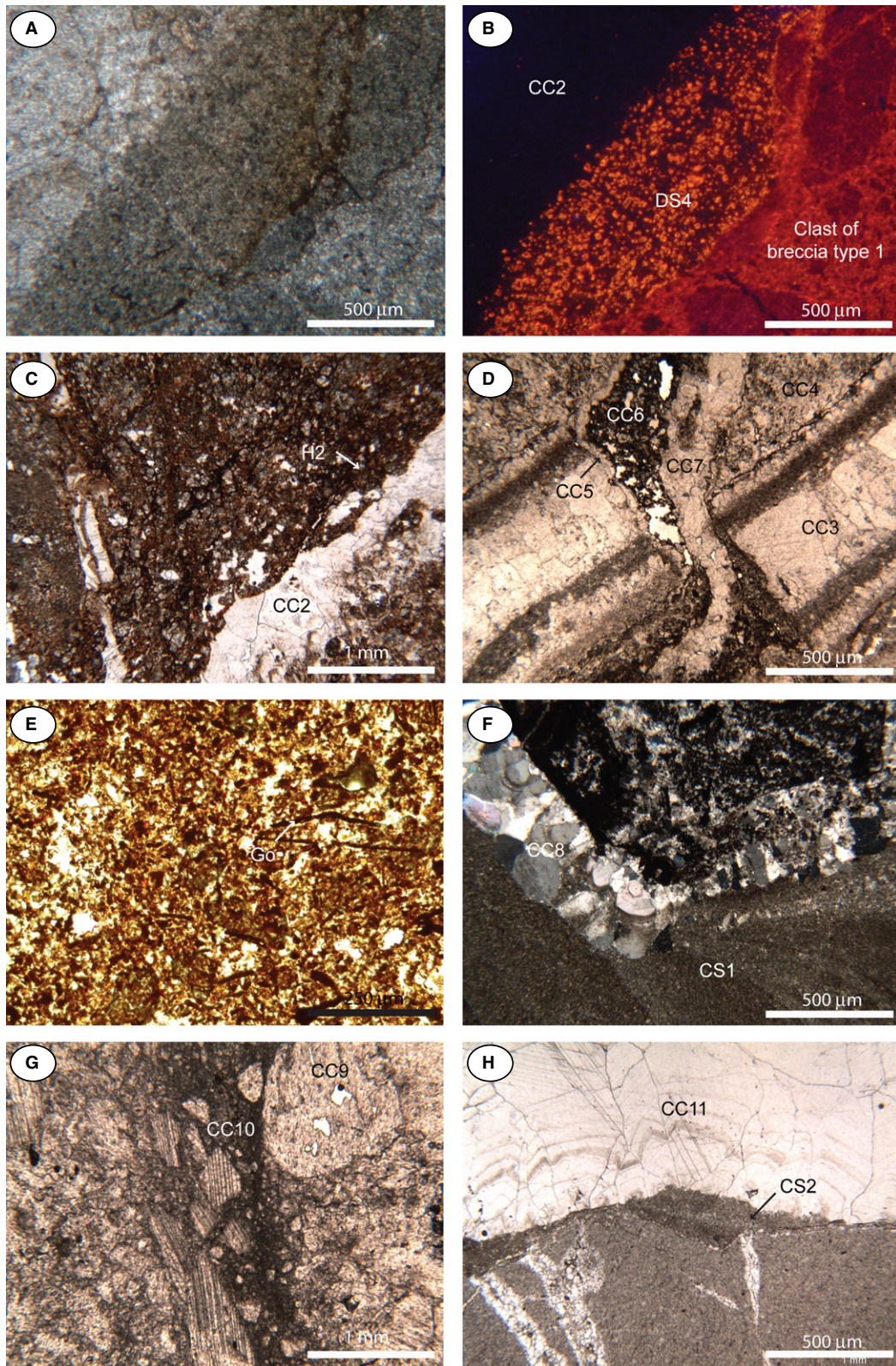


Fig. 9. (A & B) Breccia type 3 with dolomitic sediment DS4 and calcite cement CC2; (C) Matrix of breccia type 4 with hematite cement H1; (D) Breccia type 5 with calcite cements from CC3 to CC7; (E) Calcite cement CC4 with goethite inclusions; (F) Spelean pisoids with calcite cement CC8 and calcite sediment CS1; (G) Crushed spelean pisoids with calcite cement CC10; (H) Laminated sediment CS2 and calcite cement CC11.

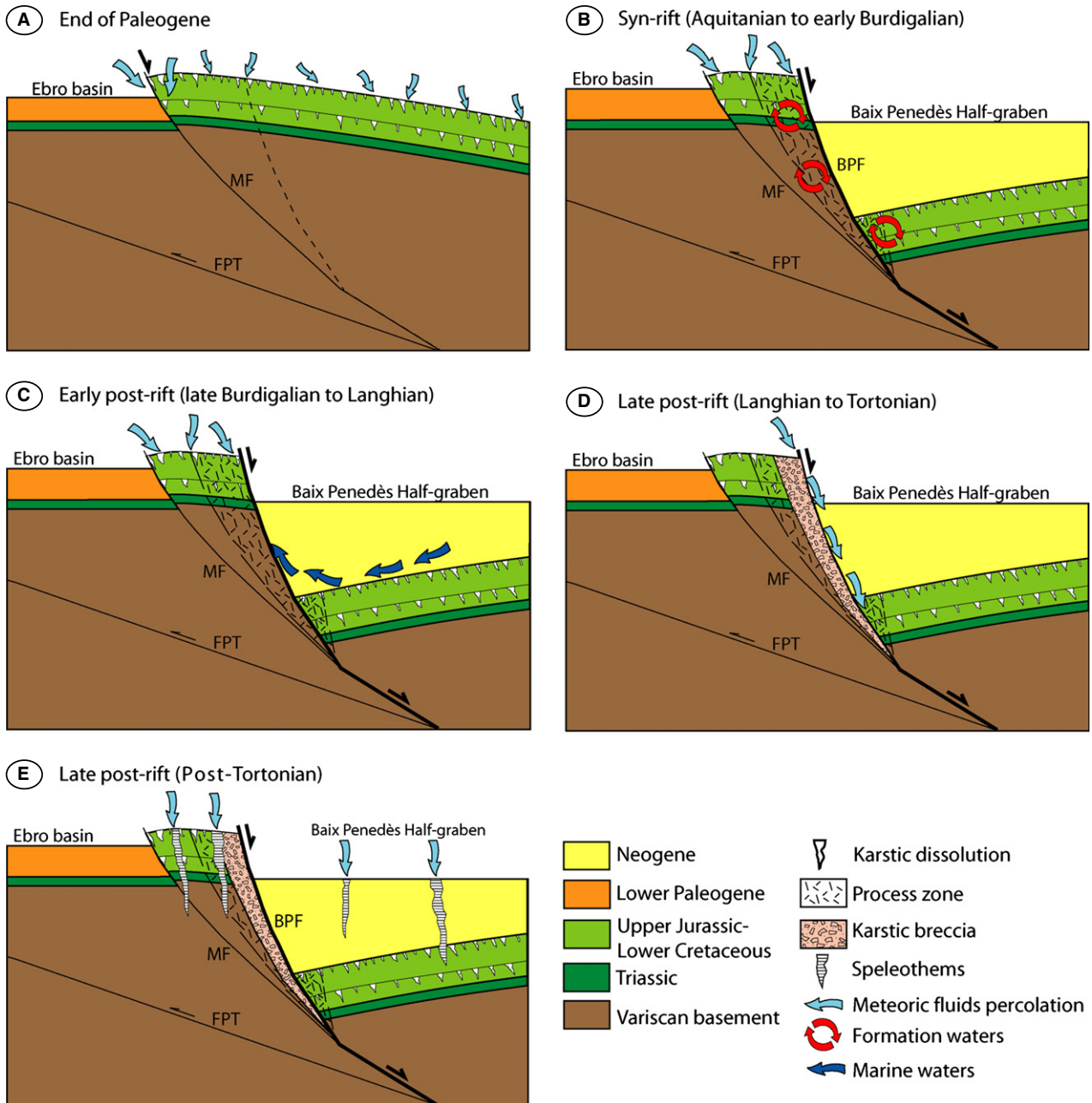


Fig. 10. Evolution of fluids from Mesozoic to post-Tortonian times within the Baix Penedès Fault. MF: Montmell Fault; FPT: Frontal Paleogene Thrust; BPF: Baix Penedès Fault.

position varies from 39.17 to 40.32% for Ca and 0.04 to 0.15% for Mg. Its Na, Mn, Fe, and Sr contents range from below the detection limit to 327, 160, 541 and 619 ppm respectively (Table 3).

Spelean pisoids, calcite cement CC8 and laminated sediment CS1

Above the type 5 breccias, there is a layer formed by laminated spelean pisoids (Fig. 4D) (Flügel 2004). The nucleus

of the pisoids corresponds to fragments of the dolomite sediments, cements, and type 5 breccia, all cemented together by bladed calcite cement CC8 arranged in a rim position and surrounded by laminated calcite sediment CS1. Calcite cement CC8 consists of nonluminescent bladed crystals, 300 μm to 1 mm in size. Its $\delta^{18}\text{O}$ varies from -8.7 to -8.6 VPDB and $\delta^{13}\text{C}$ from -7.7 to -7.4 ‰ VPDB (Fig. 7 & Table 1). Its elemental composition is between 39.72 and 40.47% Ca and 0.17 and 0.39% Mg with Na, Fe, and Mn contents ranging from below the

detection limit to 253, 216, and 501 ppm, respectively. The Mn content is always below detection limit (Table 3). Calcite sediment CS1 is formed by nonluminescent blocky anhedral calcite crystals, 4–10 μm in size. The $\delta^{18}\text{O}$ values of this sediment range from -8.6 to -8.5 ‰ VPDB and $\delta^{13}\text{C}$ from -7.8 to -7.6 ‰ VPDB (Fig. 7 & Table 1). The elemental composition is between 39.1 and 40.01% Ca, 0.19–0.36% Mg, and from 212 to 2885 ppm Fe. Na and Sr contents range from below the detection limit to 310 and 686 ppm, respectively. The Mn content is always below detection limit (Table 3).

Well-rounded spelean pisoids and calcite cements CC9 and CC10

The upper layer corresponds to a tabular white layer made up of well-rounded spelean pisoids (Fig. 4E), 0.5–10 cm in size, and cemented by calcite cement CC9 (Fig. 4F) consisting of nonluminescent drusy euhedral crystals 50 μm to 1 mm in size (Fig. 9G). $\delta^{18}\text{O}$ values vary from -8.8 to -8.1 ‰ VPDB and $\delta^{13}\text{C}$ from -7.9 to -7.8 ‰ VPDB (Fig. 7 and Table 1). The elemental composition is between 38.15 and 40.29% Ca and 0.11 and 1.13% Mg with Na, Mn, Fe, and Sr contents ranging from below the detection limit to 452, 297, 842, and 2146 ppm, respectively (Table 3). Later movements of the extensional faults generated the fragmentation of the spelean pisoids (Fig. 4G). The cataclastic-like material, formed by small fragments of spelean pisoids, is cemented by calcite cement CC10 (Fig. 9G). $\delta^{18}\text{O}$ values vary from -8.4 to -8.1 ‰ VPDB and $\delta^{13}\text{C}$ from -7.9 to -7.7 ‰ VPDB and $^{87}\text{Sr}/^{86}\text{Sr}$ ratio from 0.708102 to 0.708253 (Figs. 7–8 & Tables 1–2).

Laminated calcite sediment CS2 and calcite cement CC11

Dissolution processes enlarged the NNW-SSE fractures leading to sharp and undulating fracture walls separated up to 50 cm (Fig. 2). These fractures contain two generations of fillings. The first generation corresponds to a pink-laminated sediment (CS2) of subhedral nonluminescent crystals, 10–100 μm in size, featuring a blocky texture (Fig. 9H). The laminations correspond to size variations of the calcite crystals, and in some cases include goethite and dolomite crystals as well. $\delta^{18}\text{O}$ is -6.9 ‰ VPDB and $\delta^{13}\text{C}$ -8 ‰ VPDB (Fig. 7 & Table 1). The elemental composition is between 38.83 and 39.43% Ca and 0.31 and 0.49% Mg with Na, Fe, and Sr contents ranging from below the detection limit to 163, 561, and 1207 ppm, respectively. Mn content is always below the detection limit (Table 3). The second filling phase corresponds to calcite cement CC11, made up of bladed nonluminescent crystals from 50 to 250 μm in size (Fig. 9H). $\delta^{18}\text{O}$ values vary from -8.8 to -6.5 ‰ VPDB and $\delta^{13}\text{C}$ from -9.6 to -7.8 ‰ VPDB (Fig. 7 & Table 1).

The elemental composition is between 38.59 and 40.23% Ca, 0.11 and 0.82% Mg, and between 1126 and 1510 ppm Sr with Na and Fe contents ranging from below the detection limit to 211 and 1103 ppm, respectively. Mn content is always below detection level (Table 3). This cement has a palisade texture developing up to 30 cm in thickness. Sometimes this cement fills the remaining fracture porosities of the earlier stages.

DISCUSSION

The different field characteristics of the three outcrops studied indicate that the three fault zones correspond to three different segments of the fault, which were temporarily connected and disconnected during the Neogene allowing different diagenetic processes to occur. Below we summarized our interpretation of the evolution of the Baix Penedès Fault (Fig. 10). Also, we attempt to explain how the dissolution processes were affected by the different stages of fracturing during the upward fault-tip propagation. The study of the fractures was combined with petrographic and geochemical analysis of the fracture-filling cement phases in order to identify the type of the fluids they were precipitated from.

Diagenesis of the host rock

The $\delta^{18}\text{O}$ values of the host rock (RD1), which range from -2.1 to $+1.2$ ‰ VPDB, show clear marine influence during the dolomitization process (Budd 1997). These values, together with the $\delta^{13}\text{C}$ and $^{87}\text{Sr}/^{86}\text{Sr}$ data, suggest that dolomitization took place in Upper Jurassic-Lower Cretaceous times (Veizer *et al.* 1999). Nadal (2001) has argued that the interval of time from the Thitonian to Berriassian was a period of dolomitization that affected the central part of the Catalan Coastal Ranges (CCR) and neighboring areas.

Stage A: Diagenetic processes related to the end of Paleogene

Dolomitic sediment DS1, filling the initial vuggy porosity, has petrographic characteristics and $\delta^{18}\text{O}$ values similar to those of host-dolomite RD1. This suggests that DS1 comes from the erosion and reworking of the host rock. However the dolomitic sediments are more depleted in $\delta^{13}\text{C}$, indicating that the sediment was further altered on contact with a fluid more enriched in organic CO_2 (Moore 2001). This dissolution event can be related to the extensive dissolution that took place in the area during and after the uplift of the CCR due to Paleogene compression (Cabrera 1981; Albaigés *et al.* 1985; Esteban 1991).

Stage B: Diagenetic processes related to Miocene (Aquitainian? to early Burdigalian) syn-rift stage

Due to the initial upward propagation of the Baix Penedès fault, deformation was characterized by random-fracture fabrics cemented by dolomitic cement DC1. The $\delta^{18}\text{O}$ values of this cement, varying between -2.3 and -1.3 ‰ VPDB (Table 1). This is evidence of low temperature precipitation, which is consistent with the results of thermochronology in the central part of the CCR, which indicates that the exhumed normal fault footwall never exceeded 2 km maximum burial depth (Juez-Larré & Andriessen 2006). At Castellví and Casetes de Gomila outcrops, the host rock is partially replaced by dolomite RD2. The petrography and geochemistry of this dolomite suggest that dolomitization occurred during progressive burial of the Jurassic rocks (Tucker & Marshall 2004).

A forced fold-related fault formed within the footwall. Intense dissolution occurred along the fractures during the folding. Geochemical and isotopic data indicate that uplift associated with this deformation resulted in a period of subaerial exposure (Sharp *et al.* 2000). The $\delta^{18}\text{O}$ values of the dolomitic sediments DS2 and DS3 together with their Sr/Ca ratio (Table 3) show a similarity with the host rock. In contrast, the more depleted values of $\delta^{13}\text{C}$ could indicate the influence of soil-derived CO_2 , which suggesting the opening of the system to meteoric waters (Moore 2001).

Stage C: Diagenetic processes related to the Miocene (late Burdigalian to Langhian) early postrift stage

The $\delta^{18}\text{O}$ and $\delta^{13}\text{C}$ values, together with the Sr/Ca molar ratios of dolomite cement DC3 (Table 3), are consistent with precipitation under the influence of low-temperature marine water (Table 1) (Budd 1997). The similarity of the $\delta^{18}\text{O}$, $\delta^{13}\text{C}$, and $^{87}\text{Sr}/^{86}\text{Sr}$ values of this DC3 cement with those of DC2 (which overgrows DS2), and with those of DS3, all showing a marine signature (Veizer *et al.* 1999), suggests that the karstic sediments were dolomitized under the influence of late Burdigalian-Langhian marine waters. This resulted in the deposition of sabhka, carbonate platforms, siliciclastic and bay facies (Cabrera *et al.* 1991; Cabrera & Calvet 1996). Expulsion of the trapped marine waters and its circulation through faults would have produced dolomitization of the karstic sediments at this time (Calvet *et al.* 2001). Similar values are reported for the same type of sediments deposited in the Casablanca oil reservoir (Rodríguez-Morillas *et al.* 2013).

Stage D: Diagenetic processes related to the Miocene (Serravallian to Tortonian) late postrift stage

Uplift along normal faults created subaerial conditions and provided conduits for shallow meteoric recharge.

Meteoric fluids deposited calcite cements filling the NE–SW normal faults (CC1–CC10) correspond to a combination of tectonic and karstic processes. The $\delta^{18}\text{O}$ values of the calcite cements, together with the Mg/Ca and Sr/Ca molar ratios, and the high radiogenic values of the calcite cementing the crushed spelean pisoids, indicate that meteoric waters, rather than the interaction of marine fluids, were responsible for precipitation of the calcite cements. The oscillations in $\delta^{13}\text{C}$ values suggest that the cements were influenced by variations of the phreatic level during their deposition (Longman 1980).

Stage E: Post-Tortonian diagenetic processes

The late NNW-SSE fractures are attributed to a late post-rift stage Neogene extensional event. This resulted in tensional deformation of the whole area during the final stages of the basin development. The calcite cement CC11 that covers the fracture walls is interpreted as speleothems formed in the vadose meteoric environment, similar to those described by Calvet *et al.* 2000 and Travé & Calvet (2001). The post-Tortonian prevalence of the vadose meteoric environment is attributed to the Messinian sea-level drop (Bini *et al.* 1978; Julian & Nicod 1984; Bini 1994; Clauzon *et al.* 1997).

CONCLUSIONS

The successive deformation stages and the related karst fillings deposits/cements described above allowed us to identify four different events of karstification: (i) Karstification related to the Paleogene compression characterized by widespread dissolution and the generation of vug and cavern porosity due to subaerial exposure of the Mesozoic carbonates. Geochemistry of the cements and sediments filling this porosity indicates that they originated from the erosion and reworking of the host rock. (ii) Karstification related to the syn-rift (Neogene) extension occurring mainly along fractures, promoting the propagation of the Neogene faults. Geochemistry of the different types of dolomitic karst-fill sediments occurring also in the fracture porosity indicates that they were deposited from a meteoric fluid in an open hydrological system. $^{87}\text{Sr}/^{86}\text{Sr}$ data suggest, however, that these sediments were later dolomitized under the influence of late Burdigalian-Langhian marine waters. (iii) Karstification occurs during the transition between the syn- and postrift Neogene extension and affects some of the resulting horsts. The calcite fillings related to the NW-SE normal faults are mixtures of tectonic and karstic processes and resulted from multi-stage movement of the faults during rifting. The $\delta^{18}\text{O}$ values, together with the Mg/Ca and Sr/Ca molar ratios of the calcite cements and the high radiogenic values of the cal-

cite cementing of the crushed spelean pisoids, indicate that meteoric waters not equilibrated with the host limestone were responsible for the precipitation of these cements. The karst filling of this third event was clearly affected by the normal faults and by the strike-slip faults, suggesting that it developed during the syn- and postrift stages. (iv) Karstification promoted by the NNW-SSE trending fractures related to the late postrift. Calcitic sediments and cements, interpreted as speleothems, cover the fracture walls. The low $\delta^{13}\text{C}$ of these speleothems indicates a higher involvement of soil-derived CO_2 and precipitation in the vadose meteoric environment. The karstic fillings of this fourth event are not deformed and are attributed to the Neogene postrift. The observed multiphase karstification and cementation events related to the Baix Penedès Fault must be taken into consideration when interpreting the karstified limestones offshore, as different episodes of fluid migration, either enhancing or reducing the reservoir porosity, probably occurred as well offshore, where Mediterranean oilfields developed, as has been demonstrated in this onshore analog.

ACKNOWLEDGEMENTS

The isotopic and electron microprobe analyses were carried out at 'Centres Científics i Tecnològics' of the Universitat de Barcelona and the strontium analyses at SGIker Geochronology department of the Facultad de Ciencia y Tecnología-Universidad del País Vasco/EHU. We wish to thank Jordi Illa for technical support. We also thank to valuable comments and suggestions of the reviewers and the editor Mark Pearson and to Frances Luttkhuizen for the revision of the English version. This research was performed within the framework of I + D + I research projects CGL2010-18260 of the Grup Consolidat de Recerca 'Geologia Sedimentària' (2009 SGR-1458), the BES-2007-14935 grant.

REFERENCES

- Agustí J, Cabrera L, Moya S (1985) Sinopsis estratigràfica del Neògeno en la fosa del Vallès-Penedès. *Paleontologia Evolutiva*, **18**, 57–81.
- Albaigés J, Borbon J, Walker IW (1985) Petroleum isoprenoid hydrocarbons derived from catagenetic degradation of Archaeobacterial lipids. *Organic Geochemistry*, **8**, 293–7.
- Anadón P, Cabrera L, Guimerà J, Santanach P (1985) Paleogene strike-slip deformation and sedimentation along the southeastern margin of the Ebro Basin. In: *Strike-slip deformation, basin formation and sedimentation* (eds. Biddle KT, Christie-Blick N). *SEPM Special Publication*, **37**, 303–18.
- Ashauer H, Teichmüller R (1935) Die Variscische und Alpidische Gebirgsbildung Kataloniens. *Abh. Ges. Wiss. Göttingen math-phys.* **3** (10), 115 p. (spanish traduction: *Publ. Extr. Geol. Esp.* t. 111, CSIC).
- Audra P, Mocochain L, Camus H, Gilli E, Clauzon G, Bigot J-Y (2004) The effect of the Messinian Deep Stage on karst development around the French Mediterranean. *Geodinàmica Acta*, **17**, 389–400.
- Baqués V, Travé A, Benedicto A, Labaume P, Cantarero I (2010) Relationships between carbonate fault rocks and fluid flow regime during propagation of the Neogene extensional faults of the Penedès basin (Catalan Coastal Ranges, NE Spain). *Journal of Geochemical Exploration*, **106**, 24–33.
- Bartrina MT, Cabrera L, Jurado MJ, Guimerà J, Roca E (1992) Evolution of the central Catalan margin of the Valencia trough (western Mediterranean). *Tectonophysics*, **203**, 219–47.
- Bellahsen N, Daniel JM (2005) Fault reactivation control on normal fault growth: an experimental study. *Journal of Structural Geology*, **27**, 769–80.
- Bini A (1994) Rapports entre la karstification périméditerranéenne et la crise de salinité du Messinien: l'exemple du karst lombard, Italie (Relations between perimediterranean karstification and the Messinian crisis: the Lombardy karst example, Italy). *Karstologia*, **23**, 33–53.
- Bini A, Cita MB, Gaetani M (1978) Southern Alpine lakes: hypothesis of an erosional origin related to the Messinian entrenchment. *Marine Geology*, **27**, 271–88.
- Budd DA (1997) Cenozoic dolomites of carbonate islands: their attributes and origin. *Earth-Science Reviews*, **42**, 1–47.
- Burke WH, Denison RE, Hetherington EA, Koepnick RB, Nelson HF, Otto JB (1982) Variation of seawater $^{87}\text{Sr}/^{86}\text{Sr}$ throughout Phanerozoic time. *Geology*, **10**, 516–19.
- Cabrera L (1981) Estratigrafia y características sedimentológicas generales de las formaciones continentales del Mioceno de la cuenca del Vallès-Penedès (Barcelona, España). *Estudios Geológicos*, **37**, 35–43.
- Cabrera L, Calvet F (1996) Onshore Neogene record in NE Spain: Vallès-Penedès and el Camp half-grabens (NW Mediterranean). In: *Tertiary Basins of Spain* (eds Friend PT, Dabrio C), pp. 97–105. Cambridge University Press, Cambridge.
- Cabrera L, Calvet F, Guimerà J, Permanyer A (1991) El registro sedimentario miocénico en los semigrabens del Vallès-Penedès y del Camp: organización secuencial y relaciones tectónica sedimentación. *I Congreso del Grupo Español del Terciario. Libro-guía Excursión*, **84**, 132 pp.
- Caine S, Evans JP, Craig BF (1996) Fault zone architecture and permeability structure. *Geology*, **24**, 1025–8.
- Calvet F, Canals A, Cardellach E, Carmona JM, Gómez-Gras D, Parcerisa D, Bitzer K, Roca E, Travé A (2000) *Fluid Migration and Interaction in Extensional Basins: Application to the Triassic and Neogene Rift in the Central Part of the Catalan Coastal Ranges*. NE Spain, Field Gríde III Geofluids Congres. 58 pp.
- Calvet F, Travé A, Bitzer K, Roca E, Tritlla J, Baker J (2001) Dolomitization of detrital deposits related to Neogene extensional faults, Catalan Coastal Ranges (Spain). *Geotemas*, **3**, 109–11.
- Clauzon G, Rubino JL, Casero P, (1997) Regional modalities of the Messinian Salinity Crisis in the framework of two phases model. In: *Neogene basins of the Mediterranean region: controls and correlation in space and time*, *R.C.M.N.S. Inter-Coll.*, Catania, Program and Abstracts; 44–6.
- Clavell E, Berastegui X (1991) Petroleum geology of the Gulf of Valencia. *Publicación Especial de la Asociación Europea de Geocientíficos Petroleros*, **1**, 355–68.
- Claypool GE, Holser WT, Kaplan IR, Sakai H, Zak I (1980) The age curves of sulphur and oxygen isotopes in marine sulphate and their interpretation. *Chemical Geology (Isotope geoscience section)*, **28**, 199–260.
- Combes PJ (1969) *Recherches sur la genèse des bauxite dans le nord-est de l'Espagne, le Languedoc et l'Ariège (France)*. Tomes

- III-IV, Université de Montpellier-Faculté des Sciences, Mémoires du centre d'études et de recherches géologiques et hydrogéologiques. 335 pp.
- Coplen TB, Kendall C, Hoppo J (1983) Comparison of stable isotope reference samples. *Nature*, **302**, 236–8.
- Craig H, Gordon I (1965) Deuterium and oxygen-18 variations in the ocean and marine atmosphere. In: *Stable Isotopes in Oceanographic Studies and Paleotemperatures* (ed Tongiorgi E), pp. 9–130. Consiglio Nazionale delle Ricerche, Laboratorio di Geologia Nucleare, Pisa, Italy.
- Csoma AE, Goldstein RH, Mindszenty A, Smone L (2004) Diagenetic salinity cycles and sea level along a major regional unconformity, Mte Campo Sauro. Italy. *Journal of Sedimentary Research*, **74**/6, 889–903.
- Dickson JAD (1966) Carbonate identification and genesis as revealed by staining. *Journal of Sedimentary Petrology*, **36**, 491–505.
- Esteban M (1991) Paleokarst: case histories. In: *Paleokarsts and paleokarstic reservoirs* (eds Wright VP, Esteban M, Smart PL). Postgraduate Research Institute for Sedimentology, University of Reading PRIS Contribution, Reading, **152**, 120–46.
- Esteban M, Klappa CI (1983) Subaerial exposure environments. In: *Carbonate depositional environments* (eds Scholle PA, Bebout DG, Moore CH), pp. 1–54. Tulsa, American Association Petroleum Geologists.
- Esteban M, Wilson JL (1993) Introduction to karst systems and paleokarst reservoirs. In: *Paleokarst Related Hydrocarbon Reservoirs* (eds Fritz RD, Wilson JL, Yurewicz DA). SEPM Core Workshop Tulsa, OK, **18**, 1–9.
- Fairchild I, Smith CL, Baker A, Fuller L, Spo C, Matthey D, McDermott F (2006) Modification and preservation of environmental signals in speleothems. *Earth-Science Reviews*, **75**, 105–53.
- Flügel E (2004) *Microfacies of carbonate rocks*. Springer, Berlin-Heidelberg, 976 pp.
- Fontboté JM (1954) Las relaciones tectónicas de la depresión del Vallès-Penedes con la cordillera prelitoral y con la depresión del Ebro. Tomo Homenaje a Prof. E. Hernandez-Pacheco. Revista de la Sociedad Española de Historia Natural, 281–310.
- Gallart F (1981) Neógeno superior y Cuaternario del Penedès (Catalunya, España). *Acta Geologica Hispànica*, **16**, 151–7.
- Gascoyne M (1992) Palaeoclimate determination from cave calcite deposits. *Quaternary Science Reviews*, **11**, 609–32.
- Gaspar-Escribano J, García-Castellanos D, Roca E, Cloetingh S (2004) Cenozoic vertical motions of the Catalan Coastal Ranges (NE Spain): the role of tectonics, isostasy, and surface transport. *Tectonics*, **23**, TC1004, 18pp.
- Ginsburg RN (1957) Early diagenesis and lithification of shallow-water carbonate sediments in south Florida. In: (eds Leblank RI, Breeding JG). *Regional aspects of carbonate deposition. Society of Economic and Paleontologists and Mineralogists Special Publications*, **5**, 80–99.
- Guimerà J (2004) La Cadena Costera Catalana. In: *Geologia de España* (ed Vera JA), pp. 603–5. SGE-IGME, Madrid.
- Howarth RJ, McArthur JM (1997) Statistics from strontium isotope stratigraphy. A robust LOWESS fit to the marine Sr-isotope curve for 0–206 Ma, with look-up table for the derivation of numerical age. *Journal of Geology*, **105**, 441–56.
- James NP, Choquette PW (editors) (1988). *Paleokarst*. New York. Springer-Verlag, 416 pp.
- Juez-Larré J, Andriessen PAM (2006) Tectonothermal evolution of the northeastern margin of Iberia since the break-up of Pangea to present, revealed by low-temperature fission-track and (U-Th)/He thermochronology. A case history of the Catalan Coastal Ranges. *Earth Planetary Sciences Letters*, **243**, 159–80.
- Julian M, Nicod J (1984) Paléokarsts et paléo-géomorphologie néogènes des Alpes occidentales et régions adjacentes. *Karstologia*, **4**, 11–18.
- Katz A (1973) The interaction of magnesium with calcite during crystal growth at 25–90°C and one atmosphere. *Geochimica et Cosmochimica Acta*, **37**, 1563–68.
- Kinsman DJJ (1969) Interpretation of Sr²⁺ concentrations in carbonate minerals and rocks. *Journal of Sedimentary Petrology*, **39**, 486–508.
- Klimowitz J, Hernández E, Serrano A (2005) A field trip guide book. The Mediterranean Basin (Catalan coastal range onshore analogues). In: *Asociación de Geólogos y Geofísicos Españoles del Petróleo* (ed. W. Martínez del Olmo). AGGEP-XXV Aniversario, Madrid, 187–208.
- Krijgsman W, Hilgen FJ, Raffi I, Sierro FJ, Wilson DS (1999) Chronology, causes and progression of the Messinian salinity crisis. *Nature*, **400**, 652–5.
- Llopis-Lladó N (1947) Contribución al conocimiento de la morfoestructura de los Catalánides. *Inst. "Lucas Madalla"*, Barcelona C.S.I.C. 373 pp.
- Lomando AJ, Harris PM, Orlopp DE (1993) Casablanca field, Tarragona Basin, offshore Spain: a karsted carbonate reservoir. In: *Paleokarst Related Hydrocarbon Reservoirs* (eds Fritz RD, Wilson JL, Yurewicz DA). Core Workshop, *SEPM* **18**, 201–25.
- Longman MW (1980) Carbonate diagenetic textures from near surface diagenetic environments. *American Association of Petroleum of Geological Bulletin*, **60**, 601–21.
- Lorenz RB (1981) Sr, Cd, Mn and Co distribution coefficients in calcite as a function of calcite precipitation rate. *Geochimica et Cosmochimica Acta*, **45**, 553–61.
- Marín MA, Roca E, Rosell O, Marcuello A, Cabrera L (2008) La Falla del Montmell: un ejemplo del control ejercido por las fallas extensivas mesozoicas en la arquitectura cenozoica de las Cadenas Costaneras Catalanas. *Geotemas*, **10**, 461–4.
- Martinell J (1988) An overview of the marine Pliocene of N.E. Spain *Géol Méditerran*, **15**, 227–33.
- McArthur JM, Howarth RJ, Bailey TR (2001) Strontium isotope stratigraphy: LOWESS Version 3. Best-fit line to the marine Sr-isotope curve for 0 to 209 Ma and accompanying look-up table for deriving numerical age. *Journal of Geology*, **109**, 155–69.
- Moore C (2001) Carbonate reservoirs: porosity evolution and diagenesis in a sequence stratigraphic framework. *Developments in sedimentology*, **55**, 444 pp.
- Morrow DW (1982) Diagenesis 2. Dolomite – Part 2: dolomitization models and ancient dolostones. *Geoscience Canada*, **9**, 95–107.
- Mucci A (1987) Influence of temperature on composition of magnesian calcite overgrowths precipitated from seawater. *Geochimica et Cosmochimica Acta*, **5**, 1977–84.
- Mussman W, Montanez IP, Read F. (1988) Ordovician Knox Paleokarst Unconformity, Appalachians. In: *Paleokarst* (James NP, Choquette PW). Springer-Verlag, Berlin, 211–28 pp.
- Nadal J (2001) Estudi de la dolomitització del Juràssic Superior-Cretaci Inferior de la Cadena Ibèrica Oriental i la Cadena Costanera Catalana: relació amb la segona etapa de rift mesozoica. PhD thesis, Universitat de Barcelona, 416 pp.
- Pin C, Bassin C (1992) Evaluation of a strontium-specific extraction chromatographic method for isotopic analysis in geological materials. *Analytica Chimica Acta*, **269**, 249–55.

- Playà E, Travé A, Caja MA, Salas R, Martín-Martín JD (2010) Diagenesis of the Amposta offshore oil reservoir (Amposta Marino CS well, Lower Cretaceous, Valencia Trough, Spain). *Geofluids*, **9**, 1–19.
- Poros ZS, Mindszenty A, Molnár F, Pironon J, Györi O, Ronchi P, Szekeres Z (2012) Imprints of hydrocarbon-bearing basinal fluids on a karst system: mineralogical and fluid inclusion studies from the Buda Hills, Hungary. *International Journal of Earth Science* (Geol.Rundsch), **101**, 429–52.
- Roca E, Guimerà J (1992) The Neogene structure of the eastern Iberian margin: structural constraints on crustal evolution of the Valencia Trough (western Mediterranean). *Tectonophysics*, **203**, 203–18.
- Roca E, Sans M, Cabrera L, Marzo M (1999) Oligocene to Middle Miocene evolution of the central Catalan margin (northwestern Mediterranean). *Tectonophysics*, **315**, 209–33.
- Rodríguez-Morillas N, Playà E, Travé A, Martín-Martín JD (2013) Diagenetic processes in a partially dolomitized carbonate reservoir: casablanca oil field, Mediterranean Sea, offshore Spain. *Geologica Acta*, **11**. doi: 10.1344/0.000001833.
- Salas R (1987) *El Malm i el Cretaci Inferior Entre el Massís De Garraf i La Serra d'Espadà*. PhD thesis, Universitat de Barcelona, Barcelona, Spain.
- Salas R, Casas A (1993) Mesozoic extensional tectonics, stratigraphy and crustal evolution during the alpine cycle of the eastern Iberian Chain. *Tectonophysics*, **228**, 33–55.
- Salas R, Guimerà J, Mas R, Martín-Closas C, Meléndez A, Alonso A (2001) Evolution of the Mesozoic Central Iberian Rift System and its Cainozoic inversion (Iberian Chain). In: *Peri-Tethys Memoir 6: Peri-Tethyan Rift/Wrench Basins and Passive Margins*. (eds Ziegler PA, Cavazza W, Robertson AHF, Crasquin-Soleau S). *Mémoires Muséum D'Histoire Naturelle*, **186**, 145–85.
- Sharp IR, Gawthorpe RL, Underhill JR, Gupta S (2000) Fault-propagation folding in extensional settings: examples of structural style and synrift sedimentary response from Suez rift, Sinai. *Egypt. Geological Society of America Bulletin*, **112**, 1877–99.
- Steiger RH, Jäger E (1977) Subcommission on geochronology: convention on the use of decay constants in geo- and cosmochronology. *Earth Planet Sciences Letters*, **36**, 359–62.
- Travé A, Calvet F (2001) Syn-rift geofluids in fractures related to the early-middle Miocene evolution of the Vallès-Penedès half-graben (NE Spain). *Tectonophysics*, **336**, 101–20.
- Travé A, Calvet F, Soler A, Labaume P (1998) Fracturing and fluid migration during Palaeogene compression and Neogene extension in the Catalan Coastal Ranges, Spain. *Sedimentology*, **45**, 1063–82.
- Tucker ME, Marshall J (2004) Diagenesis and geochemistry of Upper Muschelkalk (Triassic) build-ups and associated facies in Catalonia (NE Spain): a paper dedicated to Francesc Calvet. *Geologica Acta*, **2**, 257–69.
- Tullborg EL, Drake H, Sandström B (2008) Palaeohydrology – A methodology based on fracture mineral studies. *Applied Geochemistry*, **23**, 1881–97.
- Varela J, Vicente-Bravo JC, Navarro J, Esteban M, Martínez del Olmo W (2005) The Oil Fields in the Spanish Mediterranean Sea. In: *Asociación de Geólogos y Geofísicos Españoles del Petróleo* (ed Martínez del Olmo W), pp. 121–9. AGGEP-XXV, Aniversario.
- Veizer J, Ala D, Azmy K, Bruckschen P, Buhl D, Bruhn F, Carden GAF, Diener A, Ebneth S, Goddérís Y, Jasper T, Korte C, Pawellek F, Podlaha OG, Strauss H (1999) $^{87}\text{Sr}/^{86}\text{Sr}$, $\delta^{13}\text{C}$ and $\delta^{18}\text{O}$ evolution of Phanerozoic seawater. *Chemical Geology*, **161**, 59–88.
- Vera JA, Ruiz-Ortiz PA, García-Hernández M, Molina JM (1988) Paleokarst and related sediments in the Jurassic of Subbetic Zone, Southern Spain. In: *Paleokarst* (eds James NP, Choquette J), pp. 364–84. Springer-Verlag, New, York.
- Wigley PL, Douvier JD, Dawans JM (1988) Karst and mixing-zone porosity in the amposta marino field, offshore Spain. *AAPG Bulletin*, **72**, 1031.

GEOFLUIDS

Volume 14, Number 1, February 2014

ISSN 1468-8115

CONTENTS

- 1 Pliocene sand injectites from a submarine lobe fringe during hydrocarbon migration and salt diapirism: a seismic example from the Lower Congo Basin**
D. Monnier, P. Imbert, A. Gay, R. Mourgues and M. Lopez
- 20 Polyphasic hydrothermal and meteoric fluid regimes during the growth of a segmented fault involving crystalline and carbonate rocks (Barcelona Plain, NE Spain)**
I. Cantarero, A. Travé, G. Alías and V. Baqués
- 45 On the homogeneity of fluids forming bedding-parallel veins**
A.P. Smith, M.P. Fischer and M.A. Evans
- 58 Modeling thermal convection in supradetachment basins: example from western Norway**
A. Souche, M. Dabrowski and T.B. Andersen
- 75 Development of successive karstic systems within the Baix Penedès Fault zone (onshore of the Valencia Trough, NW Mediterranean)**
V. Baqués, A. Travé and I. Cantarero
- 95 Pore-scale multiphase flow experiments in bead packs of variable wettability**
J.G. Celauro, V.A. Torrealba, Z.T. Karpyn, K.A. Klise and S.A. McKenna
- 106 Role of compressive tectonics on gas charging into the Ordovician sandstone reservoirs in the Sbaa Basin, Algeria: constrained by fluid inclusions and mineralogical data**
I. Wazir, M. Pagel, F. Tournier, E. Portier and C. Renac

WILEY
Blackwell

Geofluids is abstracted/indexed in *Chemical Abstracts*

This journal is available online at Wiley Online Library.
Visit onlinelibrary.wiley.com to search the articles and register
for table of contents and e-mail alerts.